PHYSICAL REVIEW D **110,** 044037 (2024)

Exploring pathways to forming twin stars

Mahdi Naseri[*]
Department of Astronomy, University of Arizona, Tucson, 85721 Arizona, USA

Gabriele Bozzola[†]
Department of Astronomy, University of Arizona, Tucson, 85721 Arizona, USA
and Division of Geological and Planetary Sciences,
California Institute of Technology, Pasadena, 91125 California, USA

Vasileios Paschalidis[‡]
Departments of Astronomy and Physics, University of Arizona, Tucson, 85721 Arizona, USA

(Received 19 June 2024; accepted 16 July 2024; published 19 August 2024)

A viable model for the dense matter equation of state above the nuclear saturation density includes a hadron-to-quark phase transition at densities relevant to compact objects. In this case, stable hybrid hadron-quark stars can arise. An even more interesting scenario is one where the hadron-to-quark phase transition results in the emergence of a third branch of stable compact objects (in addition to white dwarfs and neutron stars). Inherent to the presence of a third family of compact stars is the existence of twin stars—hybrid stars with the same mass as the corresponding neutron stars but with smaller radii. Interestingly, the neutron star–twin star scenario is consistent with GW170817. If twin stars exist in nature, it raises a question about the mechanism that leads to their formation. Here, we explore gravitational collapse as a pathway to the formation of low-mass twin stars. We perform fully general relativistic simulations of the collapse of a stellar iron core, modeled as a cold degenerate gas, to investigate whether the end product is a neutron star or a twin star. Our simulations show that, even with unrealistically large perturbations in the initial conditions, the core bounces well below the hadron-to-quark phase transition density, if the initial total rest mass is in the twin star range. Following cooling, these configurations produce neutron stars. We find that twin stars can potentially form due to mass loss, e.g., through winds, from a slightly more massive hybrid star that was initially produced in the collapse of a more massive core, or if the maximum neutron star mass is below the Chandrasekhar mass limit. The challenge in producing twin stars in gravitational collapse, in conjunction with the fine-tuning required because of their narrow mass range, suggests the rarity of twin stars in nature.

DOI: 10.1103/PhysRevD.110.044037

I. INTRODUCTION

One of the most important open questions in nuclear physics research is the state of matter above the nuclear saturation density, $\rho_s \approx 2.7 \times 10^{14}\ \mathrm{g\,cm^{-3}}$. The equation of state (EOS) of cold neutron-rich matter is reasonably well understood at densities below $\sim 2\rho_s$ [1–3] (see also [4–13]). Uncertainties exist even for finite-temperature dense nuclear matter; see, e.g., [14–16]. Theoretical understanding at these densities is aided by laboratory experiments involving heavy-ion collisions; see, e.g., [17–23]. However, the dense-matter cold EOS remains highly uncertain at densities of ~ 2–$40\rho_s$ because of limitations in theoretical or lattice quantum chromodynamic (QCD) approaches; see, e.g., [3,24–27]. As a result, a plethora of theoretical possibilities for how matter behaves at densities higher than $2\rho_s$ is currently allowed. In this work, we focus on the possibility that a quark deconfinement phase transition can take place at densities encountered inside compact objects.

One of the fundamental consequences of QCD is color confinement. In the absence of strong medium effects, quarks and gluons are confined inside hadrons. Quark confinement can be violated at high temperatures or high densities, leading to the formation of a new state of matter known as quark-gluon plasma [28,29]. It is currently unclear whether quark deconfinement can take place in the deep interiors of compact objects, but this possibility has been considered by a number of works (see, e.g., [30–50].

If quark deconfinement takes place at astrophysically relevant densities, an interesting scenario arises when the phase transition occurs such that a "third family" of

---

[*] Contact author: mahdinaseri@arizona.edu
[†] Contact author: gbozzola@caltech.edu
[‡] Contact author: vpaschal@arizona.edu

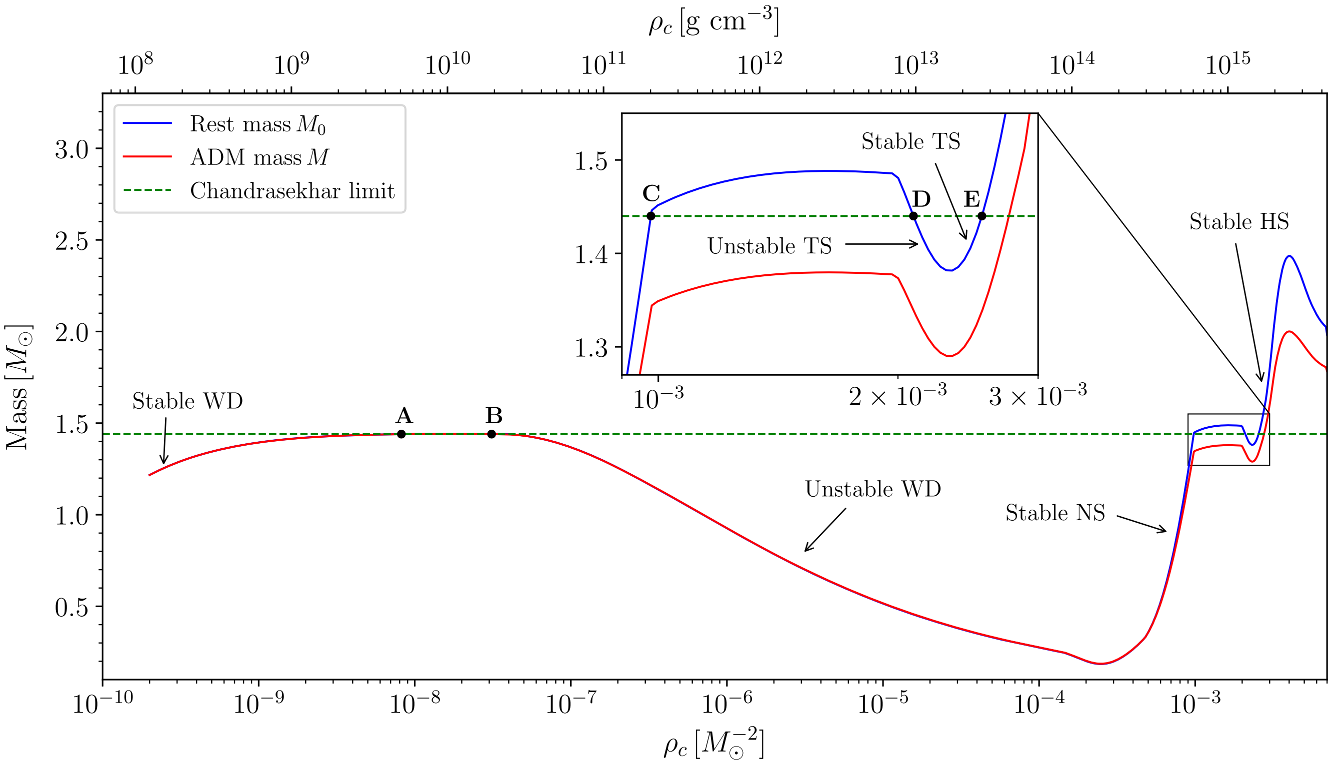

FIG. 1. Mass-central density plot for a sequence of TOV stars based on the EOS detailed in Table I. Both rest mass and gravitational (ADM) mass are illustrated. Stars with a fixed rest mass $M_0 = M_{0,s} \sim M_{\rm ch}$ are designated by labels **A**, **B**, **C**, **D**, and **E**. The inset enlarges the twin star part of the curve. More details on this plot are provided in Sec. II.

compact objects (in addition to white dwarfs and neutron stars) emerges [51–63]. Compact objects in this third family are hybrid hadron-quark stars or hybrid stars—configurations with a quark core enveloped by a hadronic shell. The stable third family of compact stars is separated from the branch of stable neutron stars (NSs) by an unstable branch of compact objects, just like stable NSs are separated from stable white dwarfs (WDs) by an unstable branch. Figure 1 depicts these branches on a mass versus central density plot (further details on this plot are discussed in Sec. II). As a result, there exists a set of stable hybrid stars (HSs) that have the same mass as NSs but smaller radii. These HSs are typically referred to as twin stars (TSs) [54,64–71]. A number of recent works suggest that current experimental and multimessenger observations of NSs are either consistent with or provide evidence in favor of the existence of hadron-to-quark phase transitions in their cores [72–77], but some works do not favor this possibility [78,79]. The third family of compact objects with potentially low-mass TSs has been shown to be consistent with a number of experiments and observations [34,67,80–85]. Twin stars are particularly interesting, because proof of their existence would provide valuable insights into the quark-gluon phase diagram.

The third family can arise when the EOS features a strong hadron-quark phase transition (i.e., characterized by a sufficiently large jump in energy density at a roughly fixed pressure) which is first order (meaning that the first derivative of free energy with respect to a thermodynamic variable is discontinuous) [53]. Alternatively, hybrid EOSs with mixed pasta phases can also lead to the formation of the third family; see, e.g., [86]. What determines the nature of the phase transition is the surface tension between the quark and hadron phases [87,88]. If the tension between these phases is low, a mixed phase of quark and nucleonic matter forms in between purely nuclear and quark matter phases. By contrast, if the tension is high, a sharp transition boundary is favorable. Both possibilities are theoretically allowed, because the surface tension is not known accurately.

Given the large number of works suggesting that hybrid and twin stars are compatible with observations, an important question arises: If these stars exist, how can they form? We begin to tackle this question in this work.

Stellar gravitational collapse appears to be a natural pathway for the formation of HSs. One might expect this, given that WDs and NSs are end points of stellar evolution; see, e.g., [89,90]. However, forming TSs through gravitational collapse faces an important challenge; if one imagines the collapse of the stellar core at approximately constant rest mass, following cooling, the configuration would contract and encounter first the branch of stable NSs, and then the branch of TSs, assuming further contraction. Thus, it is unclear whether there exists a natural pathway during stellar collapse that would prefer to form TSs over NSs. In fact, the work of [91] treated the evolution of configurations in the TS mass range that are initially on the unstable branch and found that these stars naturally transition to the stable NS branch. Thus, Ref. [91] concluded that it would be challenging to form TSs through gravitational collapse, because in a quasiadiabatic, constant rest-mass contraction of a proto-NS that is on its way to forming a TS, it would have to go through the unstable branch first, which appears to favor NSs.

The primary objective of this paper is to explore whether HSs and, in particular, TSs can form as a result of the gravitational collapse of a stellar core. To investigate this pathway toward HS formation, we perform three-dimensional hydrodynamic simulations of unstable WDs in full general relativity by considering several types of initial perturbations differing in the degree of violence of the collapse. The advantage of considering a WD for our initial conditions is that it models two distinct channels to forming neutron or hybrid stars: (i) the collapse of a degenerate iron core of a massive star and (ii) the accretion-induced collapse of a WD [92]. Here, we do not treat detailed microphysics or neutrino effects. Instead, we focus on treating properly relativistic gravitation, which is critical when compact objects arise.

Our simulations demonstrate that, for a type of EOS which gives rise to a third family of compact objects, the gravitational collapse of a WD in the twin star mass regime prefers the formation of NSs and not TSs, even under extreme initial perturbations. The only pathway to forming TSs that we were able to identify is as follows: First, a massive core should collapse to a slightly more massive stable HS, which may subsequently lose a small amount of mass, for example, in the form of winds or due to rotation or a "grazing" collision with a black hole, to ultimately settle as a TS. The results of our simulations, in conjunction with the narrow mass range over which twin stars exist, suggest that twin stars should be rare. Thus, if a HS star was involved in GW170817, then it likely was not a twin star.

The paper is structured as follows. In Sec. II, we construct the EOS that we employ in this work based on a realistic EOS with a hadron-to-quark phase transition. In Sec. III, we discuss our initial data and evolution methods along with the numerical scheme employed in the simulations. Results of various simulations exploring the formation of HSs under different conditions are presented and discussed in Sec. IV. We conclude in Sec. V, where we summarize our main findings. Unless specified otherwise, throughout this paper we adopt geometrized units where $c = G = 1$, with c being the speed of light in vacuum and G representing the gravitational constant.

II. EQUATIONS OF STATE

There exists a broad range of possibilities for the EOS in the deep interior of a NS. Numerous studies have explored different hadronic models, quark models, and hybrid hadron-quark models. For comprehensive reviews, readers are referred to [27,93–95]. Apart from microscopic, so-called realistic EOSs, the EOS can also be treated phenomenologically, e.g., by giving the pressure or sound speed as a function of rest-mass or energy density; see, e.g., [72,96–98]. Here, we restrict our discussion to the astrophysical implications of EOSs that are based on realistic models but treated phenomenologically. The EOSs we consider give rise to a third family of stable compact stars. However, to simulate the collapse of a stellar iron core or a WD, the EOSs we construct must encompass a wide range of densities, spanning the entire range from below neutron drip to the supranuclear regime. Here, we describe how we construct the phenomenological EOSs we adopt.

The EOS below the nuclear saturation density down to WD densities is reasonably well understood. Our base phenomenological EOS selected for this density regime is derived from the six-parameter piecewise polytropic EOS introduced in [99]. For the high-density regime, the EOS needs to incorporate a phase transition so that a stable HS branch exists. The high-density EOS that we adopt here is based on the T9 EOS of [91], which is a piecewise polytropic representation of the T9 EOS used in [36], which was, in turn, based on the ACS-II with $\xi = 0.90$ EOS of [34]. This EOS describes zero-temperature matter in beta equilibrium. Its hadronic part is derived from [100], the quark phase builds upon the MIT bag model [101–104], and the low-density crust component is added from the models in [105,106]. The quark phase of the original EOS adopts the constant sound speed parametrization

$$P(\epsilon) = \begin{cases} P_{\rm tr} & \epsilon_q \leq \epsilon \leq \epsilon_{\rm tr}, \\ P_{\rm tr} + c_s^2(\epsilon - \epsilon_{\rm tr}) & \epsilon \geq \epsilon_{\rm tr}, \end{cases} \tag{1}$$

where ϵ is the energy density, $P_{\rm tr} = P(\epsilon_q) = P(\epsilon_{\rm tr})$ is the pressure of the hadronic matter in the transition region $\epsilon \in [\epsilon_q, \epsilon_{\rm tr}]$, and c_s denotes the sound speed.

Given that the original T9 EOS is provided in tabulated form, we represent the high-density EOS, similar to the low-density regime, as a piecewise polytrope of the form

$$P = k_i \rho_0^{\Gamma_i}, \tag{2}$$

where ρ_0 is rest-mass density and $\rho_{0,i} \leq \rho_0 \leq \rho_{0,i+1}$ is the density range of each polytropic segment. Piecewise polytropes are frequently employed in the context of the NS EOS, as many proposed tabulated, realistic nuclear EOSs can be well fitted by them; see, e.g., [7,96,98,107].

The next step is to merge these two EOSs into one that can describe the entire range of densities relevant to compact objects. The low-density and high-density EOSs represented as $P = P(\rho_0)$ intersect at a matching density. The combined EOS should initially follow the low-density EOS and transition to the high-density EOS as the density increases beyond the matching density. To ensure a smooth transition below and above the matching density, in the density range of approximately 10^{11}–$10^{12}\ \mathrm{g\,cm^{-3}}$, we linearly interpolate between the two regimes using logarithmic pressure and density. This step yields a base EOS that covers a wide range of densities, extending from the crust of a WD to the dense core of a HS.

After we join the low- and high-density EOSs, we solve the Tolman-Oppenheimer-Volkoff (TOV) equations [89] for determining general relativistic hydrostatic equilibrium stellar configurations. We then make small modifications to the EOSs by fine-tuning the free parameters of the EOS to satisfy the following set of conditions.

1. A third family of compact objects is present.
2. A $2M_\odot$ [108–112] compact object should be allowed by the EOS.
3. The Chandrasekhar mass $M_{\mathrm{ch}} = 1.44M_\odot$ is the maximum WD mass, assuming a mean molecular weight of electrons $\mu_e = 2$.
4. For the range of densities in our simulations, the sound speed should be subluminal. The sound speed for a piecewise polytropic EOS is calculated as [96]

$$c_s = \sqrt{\frac{dP}{d\epsilon}} = \sqrt{\frac{\Gamma_i P}{\epsilon + P}}. \tag{3}$$

5. In the phase transition region, the sound speed should not be zero, because the equations of hydrodynamics would be only weakly hyperbolic (see [91] and discussion therein).
6. The dominant energy condition should be satisfied for all densities. In the case of a perfect fluid, this implies [113]

$$\epsilon \geq |P|. \tag{4}$$

Following small modifications to the piecewise polytropic parameters of our EOS such that all aforementioned conditions are met, we constructed the EOSs presented in Table I. The EOS designated as "EOS I" in the table is used throughout most of this study. "EOS II," on the other hand, is used only in one our simulations of gravitational collapse to a hybrid star above the twin star mass range. In EOS II, the maximum mass of the NS branch is slightly lower than M_{ch}, while the other characteristics are almost identical to those of EOS I. For the remainder of this paper, we always refer to EOS I in Table I unless EOS II is explicitly specified. A plot of these EOSs is provided in Appendix A.

The choice of piecewise polytropic parameters is not unique, but there is not much room for changing these parameters while still meeting all aforementioned conditions. Our goal here is not to explore all possible equations of state, because this is not feasible. However, by adopting the resulting phenomenological EOSs, we can perform our point-of-principle calculations.

TABLE I. The two families of piecewise polytropic EOS that are adopted in this work, presented as eight-branch piecewise polytropes with 16 free parameters (Γ_i, $\rho_{0,i}$, and k_1). Setting $M_\odot = 1$, the first coefficient is $k_1 = 20.7$, and the values of k_i for the other segments are determined by continuity at $\rho_{0,i}$, as given by Eq. (5).

	EOS I		EOS II	
i	Γ_i	$\log_{10}\rho_{0,i}[M_\odot^{-2}]$	Γ_i	$\log_{10}\rho_{0,i}[M_\odot^{-2}]$
1	1.5000	⋯	1.5000	⋯
2	1.3350	−9.8833	1.3350	−9.8833
3	1.1386	−7.4573	1.1286	−7.4661
4	2.3544	−3.8475	2.3144	−3.8475
5	3.3458	−3.3199	3.3858	−3.3109
6	0.2576	−3.0081	2.4957	−3.0126
7	5.1878	−2.7019	4.1878	−2.7290
8	7.6102	−2.5405	8.1102	−2.5405

In geometrized units[1] with $M_\odot = 1$, the first coefficient of the EOS in Eq. (2) is $k_1 = 20.7$. The value of k_i for $i > 1$ is determined by continuity condition at the boundary of each two neighboring segments, expressed as $P_i(\rho_{0,i+1}) = P_{i+1}(\rho_{0,i+1})$. This condition leads to

$$k_{i+1} = k_i \rho_{0,i+1}^{\Gamma_i - \Gamma_{i+1}}. \tag{5}$$

At sufficiently high densities, relevant for the most massive stellar configurations, the sound speed calculated by Eq. (3) becomes superluminal. Superluminality for ultradense matter with realistic EOSs is not uncommon. For example, it arises in the Akmal-Pandharipande-Ravenhall EOS [114], and efforts have been made to explain this behavior of c_s in high densities, e.g., in [115]. However, we checked that the sound speed never becomes superluminal in our dynamical spacetime simulations.

During the process of adjusting the EOS, we find that, in order to have heavy HSs with a maximum mass of at least $2M_\odot$, the sound speed must be large at densities corresponding to pure quark matter. This behavior aligns closely with the findings of [25,116–118] on the necessity of sound speed becoming close to the speed of light in densities of a few times ρ_s. Physically, this implies that pure quark matter at intermediate densities is strongly coupled and violates

---

[1] The conversion factor between cgs units and geometrized units with $M_\odot$ is given by $\rho_{\mathrm{cgs}} = G^{-3}M_\odot^{-2}c^6\rho_G$ for density and by $R_{\mathrm{cgs}} = GM_\odot c^{-2}R_G$ for length, where ρ_G and R_G stand for density and radius in geometrized units, respectively.

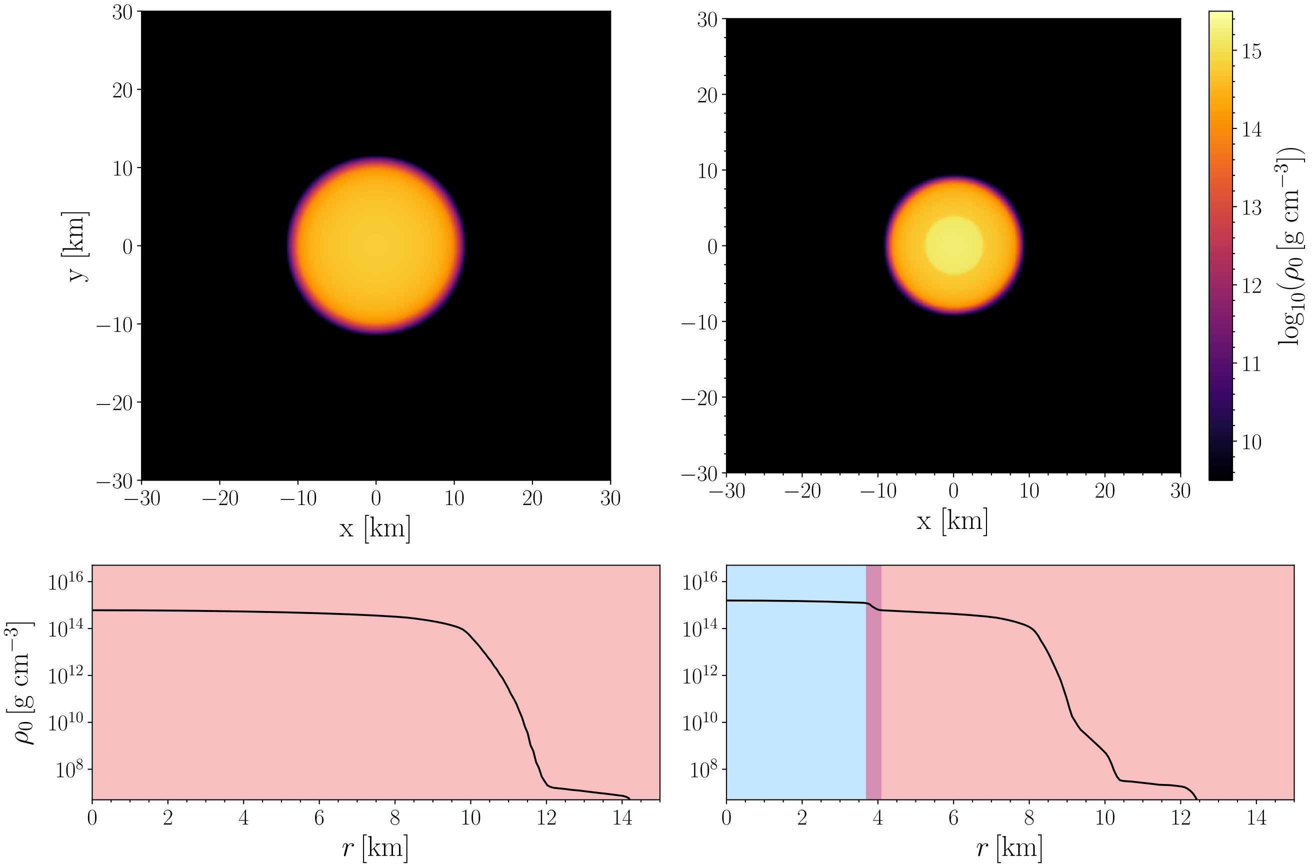

FIG. 2. A two-dimensional view (top panels) of the matter distribution inside the stable NS configuration **C** (left) and the HS configuration **E** (right). For the HS, the distinct quark core is easily distinguishable by its brighter color, indicative of the sudden increase in density. The density profile of each star is also displayed in the bottom panels as a function of the radial coordinate r. Red color in the background stands for the pure hadronic matter, blue represents the pure quark matter, and the narrow purple region in the plot of the HS density profile denotes the zone containing a mixture of quarks and hadrons.

$c_s^2 = 1/3$ predicted for asymptotically free quarks when $\rho_0 \gtrsim 40\rho_s$ [119].

With the EOS available, we solve the TOV equations for a wide range of central rest-mass densities ρ_c between 10^8 and $10^{16}\ \mathrm{g\,cm^{-3}}$. We show the resulting mass-central density plot in Fig. 1. The plot displays the total gravitational mass M, also known as the Arnowitt-Deser-Misner (ADM) mass, and the total rest mass M_0 of static stars as functions of their central rest-mass density, with red and blue curves, respectively. The branches of stable ($dM/d\rho_c > 0$) and unstable ($dM/d\rho_c < 0$) WDs, NSs, and HSs are explicitly identified based on the turning point theorem [89].

Our initial data for the collapse simulations are based on stellar configuration **B** in Fig. 1, with a rest mass $M_{0,s}$ very close to M_{ch} but on the unstable WD branch to help accelerate the collapse. The mass of this star, $1.44 M_\odot$, falls right in the mass range of TSs and allows us to perform our point-of-principle calculations to test for twin star formation. The TOV solutions with this choice of mass are labeled on this plot as $\{\mathbf{A}, \mathbf{B}, \mathbf{C}, \mathbf{D}, \mathbf{E}\}$. Configurations **A** and **B** are a stable and an unstable WD, respectively. Configurations **C** and **E** represent a stable NS and a stable HS in the twin star mass regime, respectively, although, strictly speaking, TSs have the same gravitational mass and not the same rest mass. The internal structure of these two compact stars is illustrated in Fig. 2.

The largest ADM mass is attained in our EOSs is by a HS. Stars on the unstable branch that separates stable NSs and stable HSs, such as configuration **D** (see the inset in Fig. 1), which we will refer to as unstable TSs, are entirely in the twin star mass range. Figure 1 can help visualize the basic question in our work. During the gravitational collapse of a stellar core or WD along a constant rest-mass path (dashed green horizontal line in Fig. 1), as the remnant cools it encounters first the stable NS branch and then the stable TS branch as it contracts quasiadiabatically. This begs the following question: If the NS branch is encountered first, then how can stable twin stars form?

We point out that during the evolution the remnant entropy changes due to heating; therefore, the actual evolutionary track that we describe above is not on the

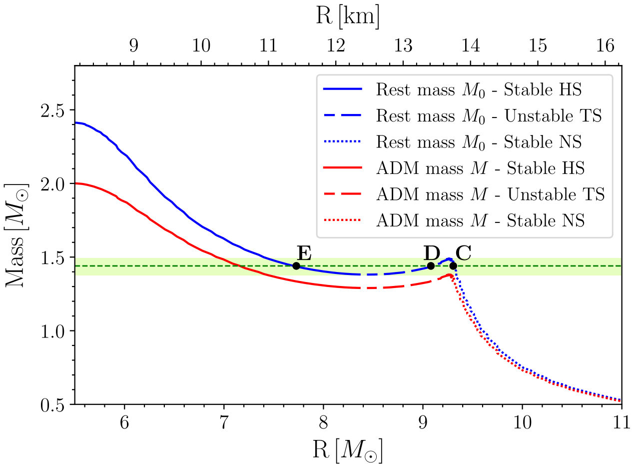

FIG. 3. Mass-radius relationship based on the EOS used in this work. Colors and points indicate the same quantities and configurations as in Fig. 1. Solid, dashed, and dotted curves stand for stable HS, unstable TS, and stable NS branches, respectively. The green shaded area represents the mass range of TSs.

plane of Fig. 1, because that corresponds to zero-entropy configurations. However, core bounce occurs above the density of the NS configuration **B**, and as the remnant cools and contracts the evolutionary path approaches the one shown by the horizontal dashed line in Fig. 1.

In addition to mass, the radius is another important macroscopic property of compact objects. For any given EOS, solving the TOV equations also determines the radius of each configuration. Consequently, every EOS has a unique mass-radius (M-R) relation that can be probed through multimessenger observations and, subsequently, impose constraints on the EOS of dense nuclear matter (see, e.g., [19,27,120–123] for reviews). The M-R relation based on our EOS is displayed in Fig. 3. The three compact stars labeled in Fig. 1 are also shown in this plot with the same labels. We show these stars on the rest-mass versus radius curve, because M_0 is conserved during collapse.

III. INITIAL DATA AND EVOLUTION METHODS

In the $M-\rho_c$ plane of Fig. 1, the unstable WD configuration **B** will collapse at constant rest mass, and, following cooling, it must ultimately migrate toward one of the two stable configurations with the same rest mass, i.e., at points **C** or **E**. During its evolution, the star moves through configurations that cannot be accurately described by cold equilibrium models, so *a priori* it is unclear which of these stable states the star will end up to. To determine the ultimate fate of the unstable WD, we perform multiple simulations of gravitational collapse by perturbing configuration **B**. As the initial configuration contracts, it heats adiabatically, and via shocks, if the core bounces. Therefore, to end up on a cold degenerate configuration, the star has to cool. We adopt a covariant local effective cooling approach, the details of which we present in Appendix B. Our cooling model is that of [124] and is characterized by a single parameter—the cooling timescale τ_c.

Except for the code that builds our tabulated EOS in Python, and our TOV solver, our computational framework is based on the Einstein Toolkit [125,126]—Cactus [127] and Simfactory [128], employing Carpet for mesh refinement [129]. Postprocessing of the simulation data is performed using the KUIBIT Python package [130].

A. Initial data

The initial data are provided by the Einstein Toolkit thorn RNSID which is based on the RNS code [131,132]. This code builds (rotating) isolated stellar configurations assuming a zero-temperature EOS in either tabulated or polytropic forms. As our EOS is represented by a piecewise polytrope I, we convert it to a highly sampled table before passing it to RNSID. For simplicity, we ignore rotation in this work.

To vary the degree of violence of the collapse of our initial configuration, we consider a set of different initial perturbations that involve nonzero velocity and/or pressure perturbations. We also consider mass depletion perturbations. We describe these below. After we impose the initial perturbations, we do not resolve the Einstein constraints, but we check in all our cases that the constraint violations are always small during the evolution.

1. Pressure perturbation

The pressure perturbations are modeled as

$$P \to (1+\xi_p)P = P + \delta P, \tag{6}$$

for every point in the configuration. Here, the value of $\xi_p = \delta P/P$ controls the strength of the perturbation. The pressure perturbation could be either negative or positive. A negative δP corresponds to pressure depletion and, consequently, speeds up the collapse. On the contrary, a positive pressure perturbation corresponds to heating the stellar interior that must be radiated away to maintain the equilibrium. We use the latter to test our implementation of effective cooling in Appendix C.

2. Velocity perturbation

Our model for velocity perturbation is given by the following two-parameter function:

$$\vec{v} \to \xi_v \left(\frac{r}{R}\right)^{\kappa} \hat{r}, \tag{7}$$

where $\vec{v}$ is the coordinate 3-velocity, $\hat{r}$ is the radial unit vector, r is the coordinate radius, R is the coordinate radius of the star, and ξ_v determines the amplitude of the velocity perturbation and could be either negative (collapsing star)

TABLE II. The set of simulations conducted in this study using EOS I is detailed below. For each case, the corresponding configuration in the $M - \rho_c$ plot for the initial data is listed, along with the perturbation parameters. The last column describes how cooling is performed during the simulation, if enabled. Further details are provided in Sec. IV. Configuration **F** represents a stable HS with $M_0 = 1.49 M_\odot$ and is discussed in Sec. IV C. The simulations based on the last two rows are presented in Appendix D.

Description	Initial TOV solution	ξ_p	ξ_m	ξ_v	κ	Cooling
Unstable WD collapse	**B**	−0.01	0.00	0.00	0.0	SI
Unstable WD collapse	**B**	−0.01	0.00	0.00	0.0	SII
Unstable WD collapse—perturbed pressure	**B**	−0.90	0.00	0.00	0.0	SI
Unstable WD collapse—perturbed pressure	**B**	−0.90	0.00	0.00	0.0	SII
Unstable WD collapse—perturbed velocity	**B**	−0.01	0.00	−0.10	0.0	⋯
Unstable WD collapse—perturbed velocity	**B**	−0.01	0.00	−0.10	0.5	SII
Unstable WD collapse—perturbed velocity	**B**	−0.01	0.00	−0.10	1.0	SII
Unstable WD collapse—perturbed velocity	**B**	−0.01	0.00	−0.10	5.0	SII
Unstable WD collapse—highly perturbed	**B**	−0.90	0.00	−0.10	0.5	SII
Unstable WD collapse—highly perturbed	**B**	−0.90	0.00	−0.10	1.0	SII
Unstable WD collapse—highly perturbed	**B**	−0.90	0.00	−0.10	5.0	SII
Unstable WD collapse—highly perturbed	**B**	−0.90	0.00	−0.30	1.0	SII
Unstable WD collapse—highly perturbed	**B**	−0.90	0.00	−0.40	1.0	SII
Stable massive HS	**F**	0.00	0.00	0.00	0.0	⋯
Massive HS—mass loss	**F**	0.00	−0.03	0.00	0.0	⋯
Stable NS	**C**	0.00	0.00	0.00	0.0	⋯
Stable HS	**E**	0.00	0.00	0.00	0.0	⋯

or positive (expanding star). The exponent κ controls the radial profile of the perturbation. The case $\kappa = 0$ is a particular model with a velocity perturbation independent of position. The choice of a power-law perturbation model is made for simplicity and is not unique. We choose $\kappa \neq 0$ so the perturbation goes smoothly to zero close to the center of the star. This is because for $\xi_v = \mathcal{O}(-0.1)$ and $\kappa = 0$ the star bounces almost immediately and explodes.

3. Mass perturbation

To simulate a configuration that experiences a small amount of mass loss, e.g., lost due to winds, the initial data are perturbed such that a low-density shell of the stellar structure is set to the tenuous atmospheric density we maintain in our simulations. This perturbation essentially changes the total rest mass as

$$M_0 \to (1 + \xi_m) M_0 = M_0 + \delta M_0. \tag{8}$$

Here, $\xi_m = \delta M_0 / M_0$ specifies the fraction of rest mass removed from or added to the original star and, hence, takes a negative value in the case of mass loss. In practice, this is done by defining a threshold rest-mass density below which the rest-mass density of the stars takes the value of the tenuous atmospheric density until the desired amount of mass δM_0 is depleted.

The parameters characterizing all simulations performed in this work are summarized in Table II.

B. Evolution

The spacetime initial data are evolved in the Baumgarte-Shapiro-Shibata-Nakamura formulation [133,134] as implemented in the public Lean code [135]. The spacetime gauge choice adopted here includes the "$1 + \log$" and the "Γ-driver" conditions [136,137]. The hydrodynamic initial data are evolved with the publicly available code IllinoisGRMHD [138,139]. We have implemented in IllinoisGRMHD the cooling of [124] that we describe in Appendix B. We also test our implementation of cooling in Appendix C. The EOS for the evolution is hybrid with a cold and thermal component:

$$P = P_{\rm cold} + P_{\rm th}, \tag{9}$$

where the cold pressure $P_{\rm cold}$ is given by EOS I or II and $P_{\rm th} = (\Gamma_{\rm th} - 1)\epsilon_{\rm th}$, with $\epsilon_{\rm th}$ being the thermal energy density. We employ $\Gamma_{\rm th} = 2$.

In the WD collapse simulations, since the radius of the initial configuration (WD) is about 100 times larger than that of the final configuration (HS or NS), it is computationally inefficient to perform the simulation with the highest resolution necessary to resolve a HS or NS from the start. Thus, we employ adaptive mesh refinement. The initial grid structure consists of two refinement levels, with the finer resolution set to 100 points across the WD. However, as the radius decreases over time (and the central density increases), the initial resolution becomes inadequate, and we add progressively higher resolution refinement levels. Based on an estimate of the final central density as $\rho_{c,f} \sim 10^{-3} M_{\odot}^{-2}$ using the equilibrium cold configurations (see Fig. 1), we construct six refinement levels that are initially inactive. As the central rest-mass density rises, these refinement levels are subsequently activated when the density reaches certain values. When all the refinement levels are activated, the highest grid resolution is 166 m. The density range between the initial central density, $\rho_{c,i}$, and $\rho_{c,f}$ is divided into six equidistant logarithmic segments. Consequently, there are seven values of density, separating these six segments, that we denote $\{\rho_1, \rho_2, \ldots, \rho_7\}$, where $\rho_1 = \rho_{c,i}$ and $\rho_7 = \rho_{c,f}$. Every time the maximum density of the star exceeds $\rho_k = (\frac{\rho_{c,f}}{\rho_{c,i}})^{1/6} \times \rho_{k-1}$ for $k = \{2, 3, \ldots, 7\}$, a new refinement level is activated. In the collapse simulations, the outer boundary is set to $1.7 R_{\mathrm{WD}} \approx 498 M_{\mathrm{WD}}$ ($R_{\mathrm{WD}} = 1058.55$ km is the initial WD radius and M_{WD} its mass). The half-side length of each new refinement level is half that of the preceding level and its resolution twice that of the preceding level. For the other simulations in this work (e.g., starting with a more massive HS), the grid has the same structure as described for the stable HS in Appendix D.

As the star collapses, it heats adiabatically, eventually resulting in a core bounce once the EOS has stiffened and significant heat has been generated. Without taking cooling into account, the collapse would stall and the star would not continue to contract to reach either of the equilibrium configurations on the TOV sequence. This excess heat is naturally radiated away in the form of neutrinos.

In the absence of a physically accurate $6+1$-dimensional neutrino code, we crudely model cooling by locally removing any excess heat, as described in Appendix B. The only free parameter that needs to be specified in this model is the cooling timescale τ_c. The value of τ_c has to be chosen such that we respect the hierarchy of timescales in our problem while also considering the duration over which the simulations can be completed. If τ_c is much larger than the dynamical timescale t_{dyn}, the computations will take a very long time to complete. However, τ_c is much smaller than t_{dyn}, which would result in rapid cooling, causing significant perturbations instead of a smoother transition to the zero-temperature remnant. As a star collapses, the density increases. Thus, the dynamical timescale of the star, defined as $t_{\mathrm{dyn}} \equiv \frac{1}{\sqrt{\rho_c(t)}}$, is not constant over time.

We follow two different strategies to activate cooling in our simulations in order to ensure that our final results are invariant with the cooling strategy. In the first strategy (SI), the collapse begins without cooling and subsequently comes to a halt due to core bounce and heat generation. When the star settles in this state, we activate cooling with $\tau_c = 3 t_{\mathrm{dyn}}$, where t_{dyn} is determined based on the central density of the settled configuration. In the second strategy (SII), cooling is activated from the beginning with $\tau_c = 3 t_{\mathrm{dyn}}$. However, as the collapse continues, τ_c is updated to track the changing dynamical timescale as the maximum rest-mass density increases. We update τ_c every time a new refinement level is added to the configuration with the same relation $\tau_c = 3 t_{\mathrm{dyn}}$, where t_{dyn} is determined based on the values of $\{\rho_1, \rho_2, \ldots, \rho_7\}$ discussed above.

IV. RESULTS

In this section, we present the results of our simulations. We begin with the simulations of WD collapse, both without and with strong initial perturbations. Subsequently, we present the outcomes of the simulation involving a HS with mass loss. Furthermore, we perform a simulation to explore the formation of a stable HS with a mass exceeding the mass range of TSs, arising from the collapse of a WD. We present how well the constraints are satisfied during the evolution in Appendix E. We also perform two simulations involving the stable NS and HS shown in Fig. 2 to demonstrate the code can reliably evolve stable stars. The results of these simulations are discussed in Appendix D.

A. White dwarf collapse

A potential pathway to forming TSs is the gravitational collapse of the iron core of a massive star or the accretion-induced collapse of a WD. An unstable WD near the Chandrasekhar limit is an acceptable model for either scenario. The initial central density and radius of the unstable WD at configuration **B** are $\rho_c = 2.14 \times 10^{10}\ \mathrm{g\,cm^{-3}}$ and $R_{\mathrm{WD}} = 1058.55$ km. Following cooling, this configuration is expected to collapse and settle into configuration **C** or **E**, since these are the only stable configurations that preserve the total rest mass. To speed up the collapse, we initially deplete 1% of the pressure at every point inside the WD, that is, $\xi_p = -0.01$.

Figure 4 shows the outcome of the simulation adopting the SII cooling strategy with four snapshots of the matter distribution. The dense core depicted in the final snapshot of this figure shows the ultimate stable compact star. The mass in the low-density region surrounding the core is negligible compared to that of the central compact object. Figure 5 presents the time evolution of the maximum rest-mass density inside the star. The horizontal orange and blue dashed lines display the central rest-mass density of the stable NS and the stable HS with the same rest mass as the initial WD, i.e., configurations **C** and **E**, respectively. The black dashed (green) curve shows the evolution of the maximum rest-mass density in the SI (SII) cooling strategy.

In both scenarios, the initial configuration slowly contracts. After $t \sim 6 t_{\mathrm{dyn}}$ (here and in Fig. 5, t_{dyn} corresponds to the dynamical timescale of the initial WD), the collapse accelerates. Around $t \sim 6.70 t_{\mathrm{dyn}}$, a bounce in the density evolution occurs, halting the rapid collapse. We note that the evolution until core bounce is insensitive to whether

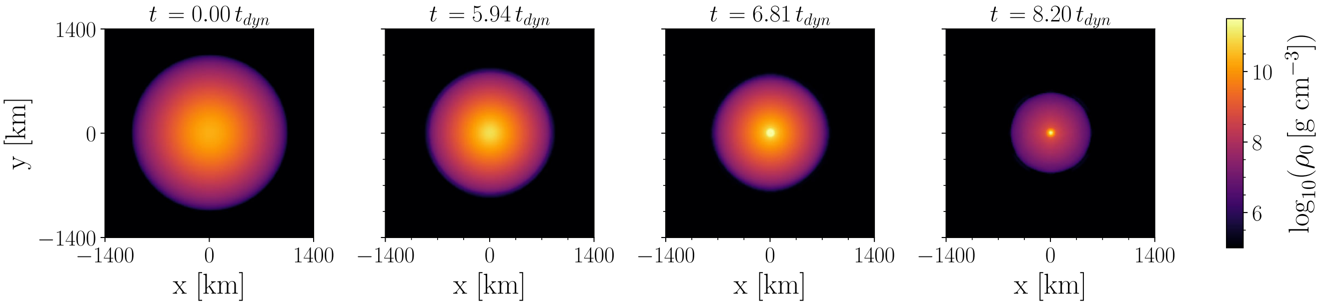

FIG. 4. Snapshots of matter distribution within the star at four different times during the collapse in the xy plane. The leftmost panel shows the unstable WD configuration **B**, and the rightmost panel shows the stable NS configuration **C**. The matter left as a low-density atmosphere around the stable NS gradually falls onto the dense core during the final stages of the collapse, but its total mass is negligible. Thus, it cannot raise the maximum density, as evidenced in Fig. 5.

cooling is active or not. After the bounce, the evolution of the maximum rest-mass density depends on the cooling strategy. In the case where cooling is initially inactive, the star settles at a density below both stable NS and stable HS. Note that this configuration does not lie on the TOV sequence with the underlying cold EOS, because it no longer has zero entropy. As soon as cooling is activated, this intermediate configuration undergoes additional collapse and asymptotes to the stable NS configuration **C** (orange dashed line). In the SII case, the star continues its collapse after the bounce, since cooling already had reduced the thermal pressure. However, the asymptotic configuration, when most of the heat has been removed, is again the stable NS configuration **C**. Thus, the outcome of the collapse is independent of the cooling strategy adopted here, and the final cold configuration has a maximum density that is below the quark-hadron phase transition region. Therefore, the final configuration is a NS.

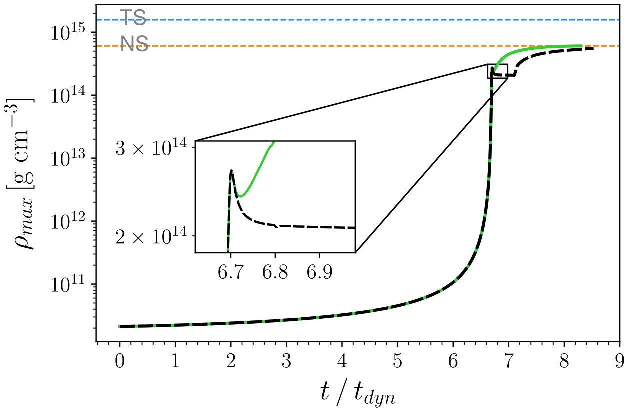

FIG. 5. Evolution of the maximum density for an unstable WD under 1% pressure depletion. Here, $t_{\mathrm{dyn}} = 26.46$ ms is the dynamical timescale of the initial WD. The orange and blue dashed lines denote the rest-mass density of the stable compact configurations **C** and **E** of Fig. 1, respectively. The black dashed (green) curve illustrates the evolutionary path in the SI (SII) cooling strategy. The inset enlarges the bounce.

We note that, in the part of the plot in Fig. 5 where the green and black curves plateau at the stable NS threshold, every unit of t/t_{dyn} corresponds to ∼170 dynamical timescales of that stable NS. Hence, the simulations were long enough to ensure that the evolution has reached the stable cold configuration.

We also conducted a simulation with $\tau_c = 1.5 t_{\mathrm{dyn}}$ as opposed to $\tau_c = 3 t_{\mathrm{dyn}}$, to check if the cooling timescale can affect the results. We confirmed that faster cooling only accelerates the collapse while leaving the final outcome unaffected. Thus, we conclude that the final product of the collapse of an unstable WD is a stable NS with the same total rest mass; these initial data do not result in a stable HS, regardless of the cooling approaches tested.

B. Strongly perturbed initial data

Here, we explore more violent perturbations to investigate whether the final remnant can be a TS if the strong bounce can be avoided or happen at a higher density past the hadron-to-quark phase transition. To cause the bounce to occur at higher densities, one can potentially think of more extreme initial conditions for the unstable WD.

1. Large pressure depletion

One of the parameters that could potentially facilitate the collapse is the strength of the pressure depletion characterized by ξ_p. A very large pressure depletion might result in a more rapid collapse. We conduct a set of simulations with SI and SII cooling beginning with configuration **B** but $\xi_p = -0.90$. While this level of pressure depletion is unlikely in nature, we use it as an extreme case to determine if collapse alone can form a TS. Since the WD is basically a Newtonian object, such a large pressure depletion has a negligible impact both on the total energy budget of the star and on the constraints.

The results of these simulations are displayed in Fig. 6. By comparing Figs. 5 and 6, it can be inferred that an exceptionally large pressure depletion accelerates the collapse substantially. In this case, the bounce occurs at

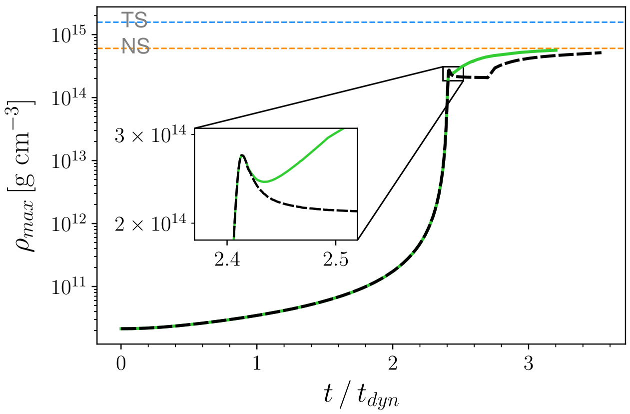

FIG. 6. The same as Fig. 5, but for the case with 90% of pressure depletion in the initial data. The line styles and colors are coded as in Fig. 5, and, similarly, $t_{\rm dyn}$ is the dynamical timescale of the initial WD.

$t \sim 2.42 t_{\rm dyn}$, almost 3 times earlier. Despite that, the core still bounces at approximately the same density and halts the collapse. Following cooling, the remnant eventually settles into a stable NS configuration. Similar to the previous set of simulations, the end product is independent of whether the SI or SII cooling strategy is adopted.

2. Velocity perturbation

Given that the binding energy of the TS is larger than that of the NS with the same rest mass, it is possible that we must inject energy into the system to overcome the bounce. One way to induce a more violent implosion is by introducing an inward velocity perturbation. This perturbation is modeled with Eq. (7), which consists of two free parameters ξ_v and κ to be specified. We fix $\xi_v = -0.1$, which corresponds to an inward velocity at the surface at 10% of the speed of light, and perform simulations with three different values of κ, namely, $\kappa = \{0.5, 1, 5\}$. Figure 7 shows the result of these simulations in the evolution plot of the maximum density, represented by maroon, green, and magenta colors, respectively.

To explore a more diverse range of initial conditions, each of these simulations is performed in two cases: $\xi_p = -0.01$ (dotted curves) and $\xi_p = -0.90$ (solid curves). In all these simulations, cooling is activated from the beginning; that is, we employ the SII cooling strategy. All these cases yield the same final result as the previous simulation of the collapsing WD; the original bounce near the last stages of the collapse is still unavoidable, and the remaining core is still a stable NS, regardless of the value of κ. Different values of κ can change only the timescale of the collapse. Among these three choices, $\kappa = 0.5$ and $\kappa = 5$ result in the fastest and the slowest processes, respectively. Moreover, the combination of the velocity perturbation with a larger pressure depletion in the initial data leads to a faster implosion in all cases.

As the last set of simulations for the collapse of an unstable WD, we also explore velocity perturbations with larger values of ξ_v. Figure 8 presents these simulations with $\xi_v = -0.3$ (dotted curve) and $\xi_v = -0.4$ (solid curve). Given that all choices of κ led to the same ultimate result, we run these simulations only for the case of $\kappa = 1$. Both simulations have 90% of pressure depletion, $\xi_p = -0.90$, and are conducted in the SII. These represent the most extreme initial conditions examined in this study. However, the result is once again the stable NS at configuration **C**. The bounce still manifests after the exponential collapse, although the process is even faster than in the previous cases. The general outcome of these simulations suggests

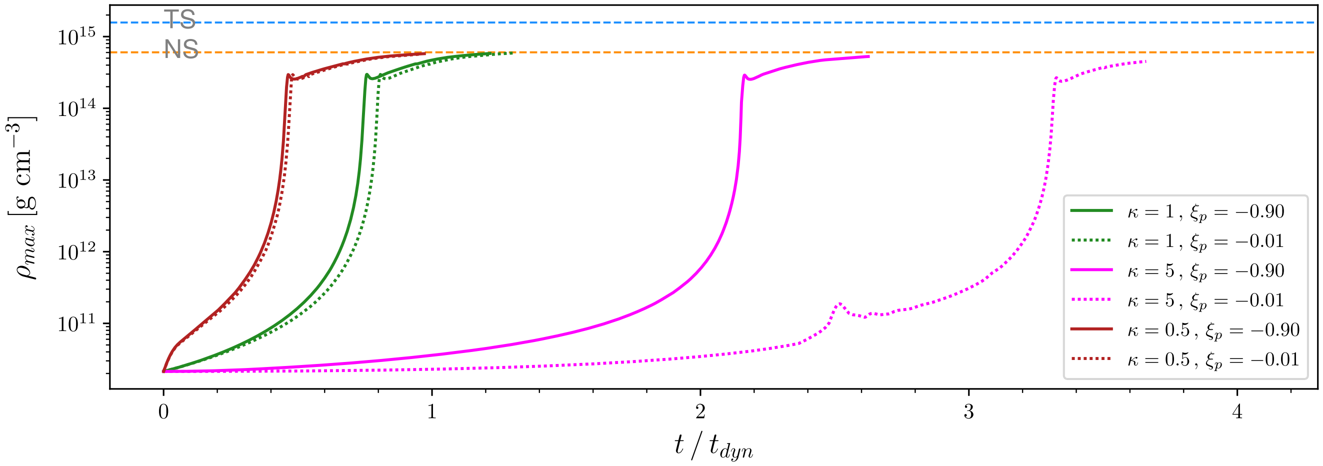

FIG. 7. Maximum density versus time for the simulations of WD implosion with initial perturbations in both velocity and pressure. Time is scaled with the dynamical timescale of the initial WD. The colors maroon, green, and magenta designate the three values of $\kappa = \{0.5, 1, 5\}$, respectively. The velocity perturbation is fixed at $\xi_v = -0.1$. Dotted lines correspond to $\xi_p = -0.01$, while solid lines to $\xi_p = -0.90$. All six simulations employ the SII cooling strategy. The dashed lines designate the central density of the stable NS or HS as in Fig. 5.

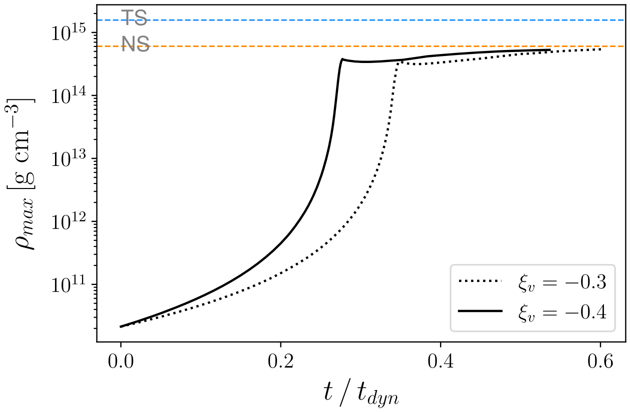

FIG. 8. The evolution of the maximum density of the collapsing WD with the most extreme initial conditions in pressure and velocity. The dotted curve shows the simulation with $\xi_v = -0.3$, and the solid curve represents the simulation with $\xi_v = -0.4$. Both the cases are performed in SII, with $\kappa = 1$ and $\xi_p = -0.90$. Similar to Fig. 5, the dashed lines show the maximum density of the stable NS or HS, and $t_{\rm dyn}$ is the dynamical timescale of the initial WD.

that even extreme pressure and velocity perturbations cannot change the eventual fate of the collapsing WD. The outcome is always a NS.

C. Mass loss

In this section, we investigate the scenario where the NS maximum mass is somewhat lower than the Chandrasekhar limit so that a stellar core or a WD at the Chandrasekhar limit collapses to the stable hybrid star branch above the twin star mass regime. If this initial hybrid star experiences some mass loss, e.g., due to strong winds, it could settle into a TS instead of a NS.

To model this scenario, we take the hybrid star configuration **F** in Fig. 9 and deplete a small fraction of its mass as described in Eq. (8). The initial rest mass of this configuration is $M_0 = 1.49 M_\odot$ and exceeds $M_{\rm ch}$. The initial central rest-mass density is $\rho_c = 1.63 \times 10^{15}\ {\rm g\,cm^{-3}}$, and the radius is $R = 11.02$ km. By setting $\xi_m = -0.033$, the rest mass of the star becomes $M_0 \approx M_{0,s}$, aligning with the rest masses of stable stars **A**, **C**, and **E** in Fig. 1. This initial perturbation is fairly strong compared to a slow loss of mass through winds, but it allows us to get a glimpse into whether this pathway to forming TSs is viable. We checked the constraint violations after the mass loss remain small throughout the simulations we performed (see discussion in Appendix E).

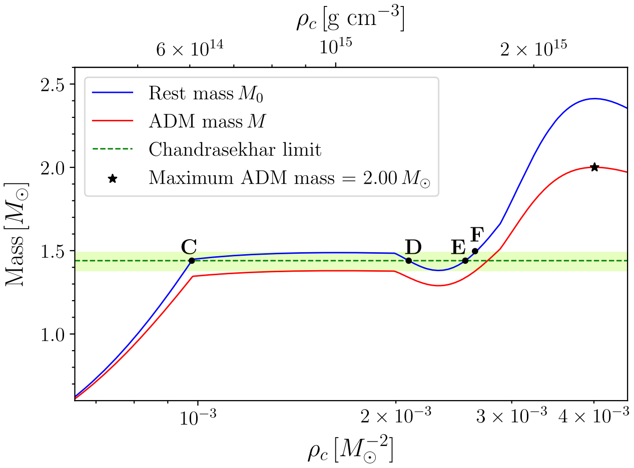

FIG. 9. An enlarged view of the NS and HS part of Fig. 1. Configuration **F** is a stable HS with a mass higher than the other three configurations indicated. The green shaded area roughly denotes the mass range for TSs. The red (blue) curve corresponds the ADM (rest) mass.

Figure 10 illustrates the results. Four simulations are shown in this figure; the stable configurations **C**, **E**, and **F** (without perturbation) are displayed by the orange, blue, and violet solid lines, respectively. The black solid curve represents the evolution of the maximum density of a star beginning at configuration **F** but perturbed by $\xi_m = -0.033$. Interestingly, this plot demonstrates that the last scenario successfully ends up with the formation of a stable HS in the twin star regime. As a result of this large initial perturbation, two types of oscillations can be seen around the maximum density of the stable HS shown in blue. The first type exhibits oscillations with a period of $\sim t_{\rm dyn}$, which gradually disappears after a few dynamical timescales. The second type of oscillation has a larger domain with $\sim \pm 10\%$ of deviations around the mean value of the central rest-mass density of the TS **E**. The latter type of oscillation has been seen before in simulations with

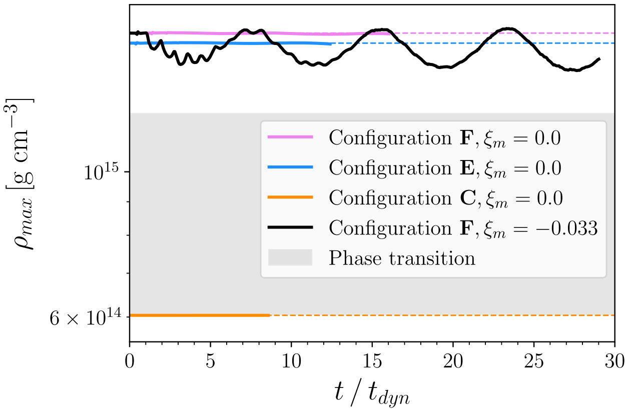

FIG. 10. Time evolution of the maximum density of configuration **F** without any perturbation (violet) and with a 3.3% mass loss (black). The stable NS and HS configurations **C** and **E** are shown in orange and blue, respectively. For each stable star, the solid line denotes the actual simulation, while the dashed line represents the initial central density. Furthermore, the shaded area indicates the density range of the phase transition. In this plot, $t_{\rm dyn}$ is the dynamical timescale of the initial HS.

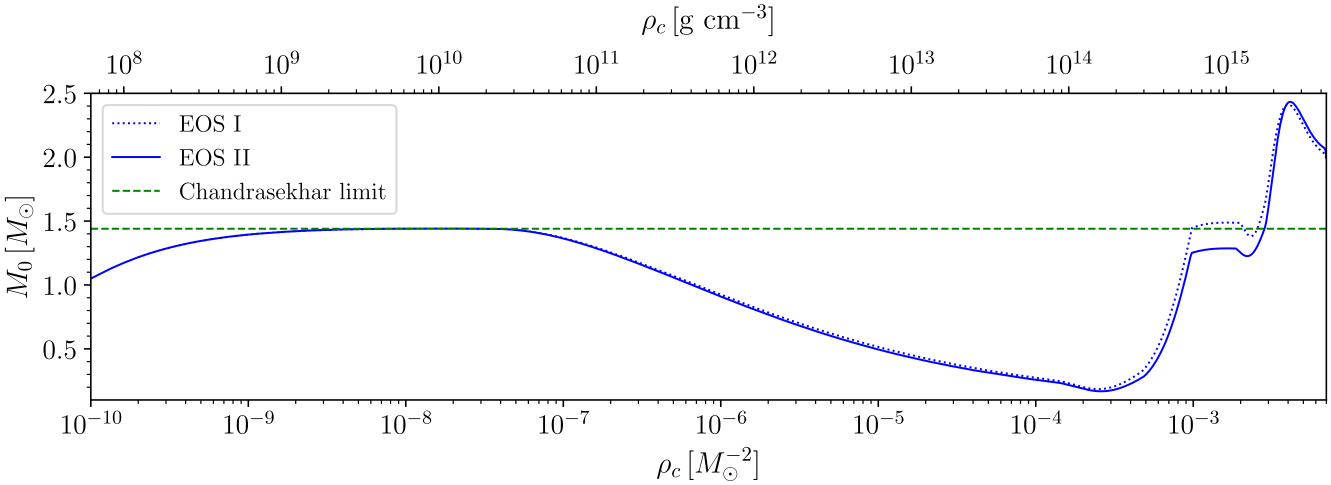

FIG. 11. Rest mass as a function of central density for a sequence of TOV stars with EOS I (dotted line) and EOS II (solid line). The dashed line represents the Chandrasekhar mass. Notably, there is no TS in EOS II with a rest mass close to M_{ch}. In the density range relevant to WDs, the two curves exhibit almost complete overlap. Thus, the initial unstable WD configuration (**B**) shares similar characteristics in both EOSs.

EOSs that exhibit a strong phase transition [91,140] and is likely due to a significant portion of the mass of the star transitioning in and out of the density range in the hadron-to-quark phase transition, where the stiffness of the EOS changes rapidly leading to collapse (EOS softens) and bounce (EOS stiffens). We expect that a gradual loss of rest mass would make such oscillations disappear, but the main result of the final configuration being a TS with the same rest mass should hold. The important finding here is that the maximum central density remains above the phase transition region as shown in Fig. 10, and its mean is that of the TS with the same rest mass.

D. Hybrid star formation

In the previous subsection, we demonstrated that TSs can form via mass loss from a more massive HS. However, this process is plausible only if a massive HS can form in the first place. In this subsection, we explore the formation of a HS with a higher mass than TSs through gravitational collapse.

The simulation we perform here is the only one in this work based on EOS II listed in Table I. Figure 11 compares the $M_0-\rho_c$ curves resulting from these two EOSs. The TOV sequence resulting from EOS II has a NS peak lower than M_{ch}. Therefore, there are no TSs with rest mass $M_{0,s}$.

Starting from an unstable WD with rest mass $M_{0,s}$ as initial data, there should be only one stable equilibrium, cold configuration at higher density. This equilibrium should correspond to a HS with a central density of $\rho_c = 1.75\times10^{15}\ \mathrm{g\,cm^{-3}}$ and a radius $R = 10.35$ km. The results of this simulation are displayed in Fig. 12, where we show the evolution of the maximum rest-mass density. The blue line denotes the described stable HS, and the shaded area shows the range of densities in the phase transition. As expected, the remnant of the collapse is this HS, as evidenced by the convergence of the maximum density to the central density of this star.

The bounce observed in the previous simulations persists in this simulation as well, due to the stiff EOS. SII cooling is employed in this simulation, starting at $\tau_c = 3t_{\mathrm{dyn}}$. When the maximum density approaches the phase transition segment of the EOS, the evolution of the maximum density becomes very slow. Since we have already confirmed that the cooling timescale does not affect the outcomes, we change the cooling timescale to $\tau_c = 1.5t_{\mathrm{dyn}}$ at $t/t_{\mathrm{dyn}} \sim 6.7$ to accelerate the transition. As the maximum density enters the segment of the EOS that softens, the configuration

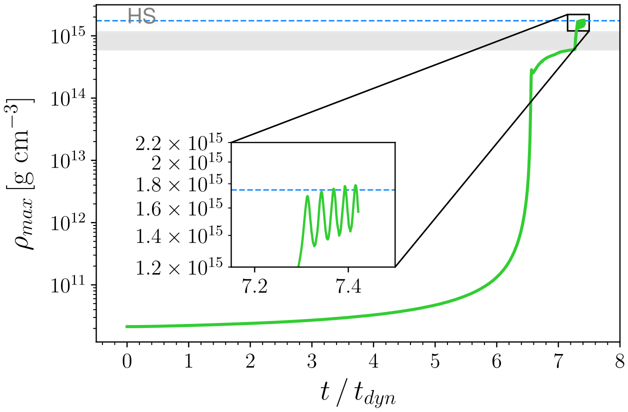

FIG. 12. The evolution of the maximum density of a star beginning as an unstable WD with a rest mass $M_0 = M_{0,s}$. The blue line represents the central density of the stable HS with this rest mass, and the phase transition range of densities is indicated by the shaded gray area. Here, t_{dyn} represents dynamical timescale of the initial WD. The inset enlarges the final stages of collapse, indicating the convergence of maximum density to the central density of the stable HS.

undergoes fast collapse to the HS formation. The only perturbation introduced in this simulation is $\xi_p = -0.01$, applied solely to speed up the initial collapse.

While not surprising, our simulations here demonstrate explicitly that forming HSs with masses higher than TSs is viable.

V. CONCLUSIONS

The exact form of the cold EOS beyond the nuclear saturation density is still quite uncertain. Cores of NSs are a common place in nature where neutron-rich matter can be found in this regime. The properties of compact stars are intricately linked to the form of the EOS at these densities. If a strong hadron-to-quark phase transition occurs at these compact star densities, the EOS can potentially give rise to a third branch of stable compact objects that consist of a quark core surrounded by a hadronic shell. These configurations are known as hybrid hadron-quark stars or hybrid stars. Associated with a third family of compact stars is a range of masses where for each NS there is a corresponding HS with the same mass but a smaller radius. These stars are referred to as twin stars.

In this work, we explored the formation of TSs by conducting hydrodynamical simulations in full general relativity. We constructed piecewise polytropic EOSs that approximate realistic EOSs with a hadron-to-quark phase transition, and we extended them down to the EOS of a white dwarf. Using our EOSs, we performed multiple simulations of the collapse of an unstable WD under different initial conditions with varying degrees of extremality of initial perturbations in pressure and/or velocity. Given that total rest mass is conserved, the ultimate product of the collapse could be either a stable NS or a stable HS. The general finding from all our simulations is that the unstable WD always collapses into a stable NS, regardless of how extreme the initial conditions are. This overall result remains the same even under extreme initial perturbations.

If TSs exist, there should be at least one pathway for them to form. Following the standard theory of NS formation, a natural path could be the formation of a more massive HS that subsequently loses a small amount of mass in the form of winds. Another potential avenue for mass loss would be a "grazing" collision of a massive HS with a black hole where the massive HS undergoes an episode of mass loss and then flies away. Such a scenario might take place in a dense stellar cluster. Our simulations show that forming HSs heavier than in the twin star mass regime is possible and that forming a TS through a heavier HS experiencing mass loss is a viable path. However, even this scenario appears that it would require some fine-tuning for TSs to form, which would place strong limits on the abundance of TSs. The fine-tuning for the formation of twin stars results because of the limited range of masses over which they are predicted to reside by existing EOSs with hadron-to-quark phase transitions, and, hence, they should be fairly rare objects. This conclusion and the challenge in producing TSs as demonstrated by our simulations suggest that if a HS star was involved in GW170817, then it likely was not a twin star.

We point out that our work is idealized in several ways and has a number of caveats. First, we do not treat realistic neutrino effects or magnetic fields, and the perturbations studied here represent a simplified version of processes that may occur inside the dense core of massive stars during the last stages of their evolution. In particular, scenarios involving mass loss due to winds and mass gain resulting from the infall of matter from outer shells of the initial progenitor are expected to happen in nature. The results of our simulations indicate that these perturbations play a notable role in the potential formation of stable TSs, assuming that they exist in nature. Thus, it is important to treat these self-consistently. Nevertheless, our conclusion that NSs tend to be the preferred outcome in the twin star mass range should hold, not only because this is what our simulations demonstrate, but also because of the very small range of masses over which twin stars are predicted to exist by current EOSs, which, in turn, requires a delicate balance of mass loss and mass gain.

To develop a more comprehensive model for the formation of TSs, further cases should be studied with a wider range of parameters. Our simulations were performed using static configurations. Rotation is another aspect that can be added with different models to future simulations to study the same problem. Additionally, these simulations were conducted considering only one type of EOS. Neutrino effects, nuclear reaction networks, and a more realistic progenitor are other ways to increase the realism of these simulations.

The effects of rotation was not treated here, but such effects on HSs have been studied [55,71,141,142]. The centrifugal barrier due to rotation is likely to lower the density compared to a nonrotating configuration for a given rest mass, thereby making matter stay well below the hadron-to-quark phase transition density. In addition, for some hybrid EOSs, rotation has the effect of increasing the neutron star maximum mass higher than that of the third family [36]. However, these results hold for cold configurations.

Temperature is another quantity that could affect stellar properties [143]; notably, phase transitions may occur at finite rather than zero temperature [144]. The EOS we adopted in this work exhibits a hadron-to-quark phase transition at zero temperature. One scenario that can potentially change the results is the possibility of an EOS with a phase transition at finite temperatures [95]. In this scenario, phase transition occurs at a lower density when the star is still hot [145]. Therefore, one can also think about the formation of TSs considering such a EOS with a finite-temperature phase transition. We will explore this possibility in future work.

Another potential pathway to forming HSs involves mergers of binary NSs or WD-NS [124,146,147] Exploring all these scenarios and including more realistic physics is left for future work. Most work in the area of TSs revolves around either observational constraints on or properties of the EOS. Our work here points out that there is another important problem surrounding TSs: their formation and abundance in nature.

ACKNOWLEDGMENTS

We thank Thomas Baumgarte for useful discussions. We are grateful to Zachariah Etienne and Leo Werneck for releasing their work on the IllinoisGRMHD code which supports piecewise polytropic EOS and to all the Einstein Toolkit developers and maintainers. We also thank Pedro Espino for sharing his EOS tables and D. Alvarez-Castillo, D. Blaschke, and A. Sedrakian for giving us permission to use the ACS-II equations of state developed in [34]. Our Python TOV solver for tabulated equations of state was developed starting from a code originally created by Nikolaos Stergioulas. Simulations were performed on the Puma cluster at the University of Arizona and on ACCESS resources under Allocation No. PHY190020. This work was supported in part by NSF Grant No. PHY-2145421 and NASA Grant No. 80NSSC24K0771 to the University of Arizona. G. B. was in part supported by the Frontera Fellowship by the Texas Advanced Computing Center (TACC). Frontera is funded by NSF Grant No. OAC-1818253.

APPENDIX A: EXTENDED EOS INFORMATION

The EOSs used in this work consist of eight segments and must satisfy the list of conditions in Sec. II. Empirically, we have found that each Γ_i controls specific characteristics of the TOV sequence shown in Fig. 1. Γ_1 primarily affects the maximum WD mass, Γ_2 alters the density and mass of the WD peak, Γ_i for $i = \{3, 4, 5\}$ controls the maximum NS mass, and Γ_6 changes the twin star mass range. Finally, Γ_i for $i = \{7, 8\}$ affects the maximum HS mass. However, it is important to emphasize that each of the free parameters affects more than just one characteristic.

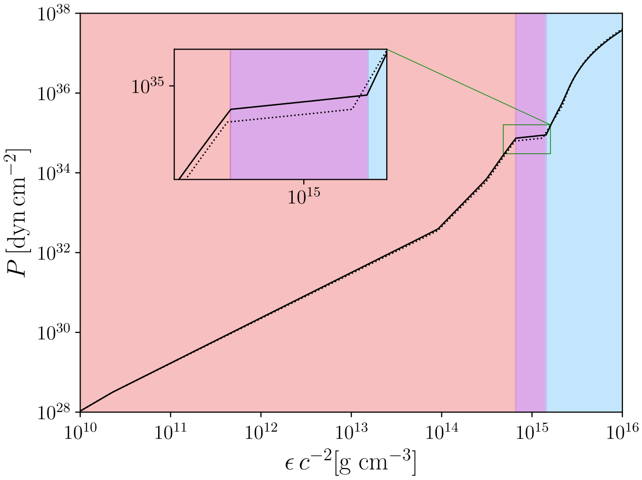

FIG. 13. The relationship between the pressure and the energy density based on the EOSs constructed in Table I. EOS I is represented by the solid line, while the dotted line denotes EOS II. The shaded red, blue, and purple areas correspond to the pure hadronic, pure quark, and the mixed quark-hadron phases for EOS I, respectively. The inset enlarges the phase transition region.

The two EOSs listed in Table I exhibit only small differences, which are mostly noticeable at higher densities. Figure 13 illustrates the pressure as a function of energy density ϵ for our EOSs. The shaded red region designates the density range where matter exists in the hadronic phase, and the blue region shows the density range where it exists purely in quark form. The narrower purple range, where the two regimes overlap ($i = 6$ branch of the EOS), is where the phase transition occurs. In this regime, the original polytropic exponent was $\Gamma_6 = 0$, corresponding to a first-order phase transition, but we modified it to $\Gamma_6 = 0.2576$ to avoid a zero sound speed. This implies that, instead of a sharp boundary from the hadron to the quark phase, there exists a mixture of hadrons and quarks in this narrow region of our EOS. This modification makes the sound speed of this region $\simeq 15\%$ of the speed of light, which allows for stable numerical integration of the general relativistic hydrodynamic equations.

APPENDIX B: COOLING FORMALISM

In this appendix, we summarize the cooling formalism adopted in our work.

In the standard $3 + 1$ decomposition formalism to numerically solve the Einstein equation, the spacetime metric $g_{\mu\nu}$ is written as follows by [148]:

$$ds^2 = -\alpha^2 dt^2 + \gamma_{ij}(dx^i + \beta^i dt)(dx^j + \beta^j dt), \tag{B1}$$

where α, β^i, and γ_{ij} are the lapse function, shift vector, and spatial metric, respectively (i and j are spatial indices). For a perfect fluid with 4-velocity u^μ, the stress-energy tensor is written as

$$T^{\mu\nu} = \rho_0 h u^\mu u^\nu + P g^{\mu\nu}. \tag{B2}$$

Here, the specific enthalpy h is related to the specific internal energy $e = \frac{\epsilon}{\rho_0} - 1$ through

$$h = 1 + e + \frac{P}{\rho_0}. \tag{B3}$$

The evolution equations for general relativistic hydrodynamics are given by [149]

$$\begin{aligned} &\partial_t\rho_* + \partial_j(\rho_* v^j) = 0, \\ &\partial_t\tilde{\tau} + \partial_i(\alpha^2\sqrt{\gamma}T^{0i} - \rho_* v^i) = s, \\ &\partial_t\tilde{S}_i + \partial_j(\alpha\sqrt{\gamma}T^j{}_i) = \frac{1}{2}\alpha\sqrt{\gamma}T^{\mu\nu}\partial_i g_{\mu\nu}. \end{aligned} \tag{B4}$$

In these equations, $v^i = u^i/u^0$ is the coordinate 3-velocity, and the conservative variables are defined as

$$\begin{aligned} \rho_* &= -\sqrt{\gamma}\rho_0 n_\mu u^\mu, \\ \tilde{S}_i &= -\sqrt{\gamma}T_{\mu\nu}n^\mu\gamma^\nu_i, \\ \tilde{\tau} &= \sqrt{\gamma}T_{\mu\nu}n^\mu n^\nu \rho_*, \end{aligned} \tag{B5}$$

where $n^\mu = \frac{1}{\alpha}(1, -\beta^i)$ is the timelike unit vector normal to $t = \text{const}$ slices.

In Eq. (B4), the first equation corresponds to the baryon number conservation. The time component of energy-momentum conservation $\nabla_\nu T_\mu{}^\nu$ is expressed in the second equation, where $s = -\alpha\sqrt{\gamma}T^{\mu\nu}\nabla_\nu n_\mu$ is a source term. The spatial components of the energy-momentum conservation are encoded in the third equation.

The set of Eq. (B4) also requires an EOS to close. The general form of the EOS that is assumed to solve this set of equations is given by Eq. (9) [150], where P_{cold} stands for the pressure of the zero-temperature matter, and has the polytropic form introduced in Sec. II. Any additional pressure due to heating, e.g., by shock heating, is encapsulated in P_{th}. This term is considered as a Γ law:

$$P_{\text{th}} = (\Gamma_{\text{th}} - 1)\rho_0 e_{\text{th}}, \tag{B6}$$

where $e_{\text{th}} = e - e_{\text{cold}}$ and e_{cold} is the specific internal energy associated with the cold pressure, which can be found from the first law of thermodynamics as

$$e_{\text{cold}}(\rho_0) = -\int P_{\text{cold}}(\rho_0)d\left(\frac{1}{\rho_0}\right). \tag{B7}$$

For the specific case of Eq. (2), this becomes

$$e_{\text{cold}} = \frac{k_i}{\Gamma_i - 1}\rho_0^{\Gamma_i - 1} + a_i, \tag{B8}$$

where a_i is a constant of integration. Considering ϵ_{cold} as the energy density when there is no heat, this constant is determined as [96]

$$a_i = \frac{\epsilon_{\text{cold}}(\rho_{0,i})}{\rho_{0,i}} - 1 - \frac{k_i}{\Gamma_i - 1}\rho_{0,i}^{\Gamma_{i-1}}. \tag{B9}$$

In the presence of radiation, the conservation of energy-momentum must be modified to incorporate the radiation stress-energy tensor $R^{\mu\nu}$:

$$\nabla_\mu(T^{\mu\nu} + R^{\mu\nu}) = 0. \tag{B10}$$

The dynamics of the radiation stress-energy tensor is described by $\nabla_\mu R^{\mu\nu} = -G^\nu$, where G^μ is the radiation four-force density. Assuming local and isotropic (in a frame comoving with the fluid) cooling, the resulting energy and momentum equations are then given by [124]

$$\begin{aligned} &\partial_t\tilde{\tau} + \partial_i(\alpha^2\sqrt{\gamma}T^{0i} - \rho_* v^i) = s - \alpha^2\sqrt{\gamma}u^0\Lambda, \\ &\partial_t\tilde{S}_i + \partial_j(\alpha\sqrt{\gamma}T^j{}_i) = \frac{1}{2}\alpha\sqrt{\gamma}T^{\mu\nu}\partial_i g_{\mu\nu} - \alpha\sqrt{\gamma}u_i\Lambda, \end{aligned} \tag{B11}$$

where we choose the same emissivity Λ as in [124]

$$\Lambda = \frac{\rho_0}{\tau_c}e_{\text{th}}. \tag{B12}$$

Here, τ_c is the cooling timescale.

Cooling changes the internal thermal energy over time. The governing equation in a comoving frame can be written as [124]

$$\frac{de_{\text{th}}}{d\tau} = \left[\frac{(\Gamma_{\text{th}} - 1)}{\rho_0}\frac{d\rho_0}{d\tau} - \frac{1}{\tau_c}\right]e_{\text{th}}, \tag{B13}$$

where τ is the proper time. When no adiabatic contraction or expansion takes place, then ρ_0 is constant, and the last equation describes an exponential evolution of e_{th} as a function of proper time, that is,

$$e_{\text{th}} \propto \exp\left(-\frac{\tau}{\tau_c}\right). \tag{B14}$$

APPENDIX C: COOLING TESTS

To validate our implementation of cooling, we introduce a uniform perturbation in pressure everywhere in a test simulation involving a stable NS. We adopt a cold polytropic function EOS, $P = k\rho_0^\Gamma$, where $\Gamma = 2$ and $k = 100M_\odot^2$. Equation (9) implies that any positive perturbation in pressure adds some P_{th} to the initial cold pressure. We conduct three different simulations for a stable NS with the central density $\rho_c = 0.001M_\odot^{-2}$. In the first simulation, no pressure perturbation is applied, and cooling remains inactive. In the second simulation, we impose a small pressure perturbation with $\xi_p = 0.01$, which consequently produces heat, but cooling is not active. Finally, we conduct a simulation that includes the same pressure perturbation as the second simulation, while cooling is active with $\tau_c = 3.16t_{\text{dyn}}$. We continue the simulations for $\sim 30t_{\text{dyn}}$.

Figure 14 shows the result of these simulations for the absolute value of e_{th} at four different times. The three

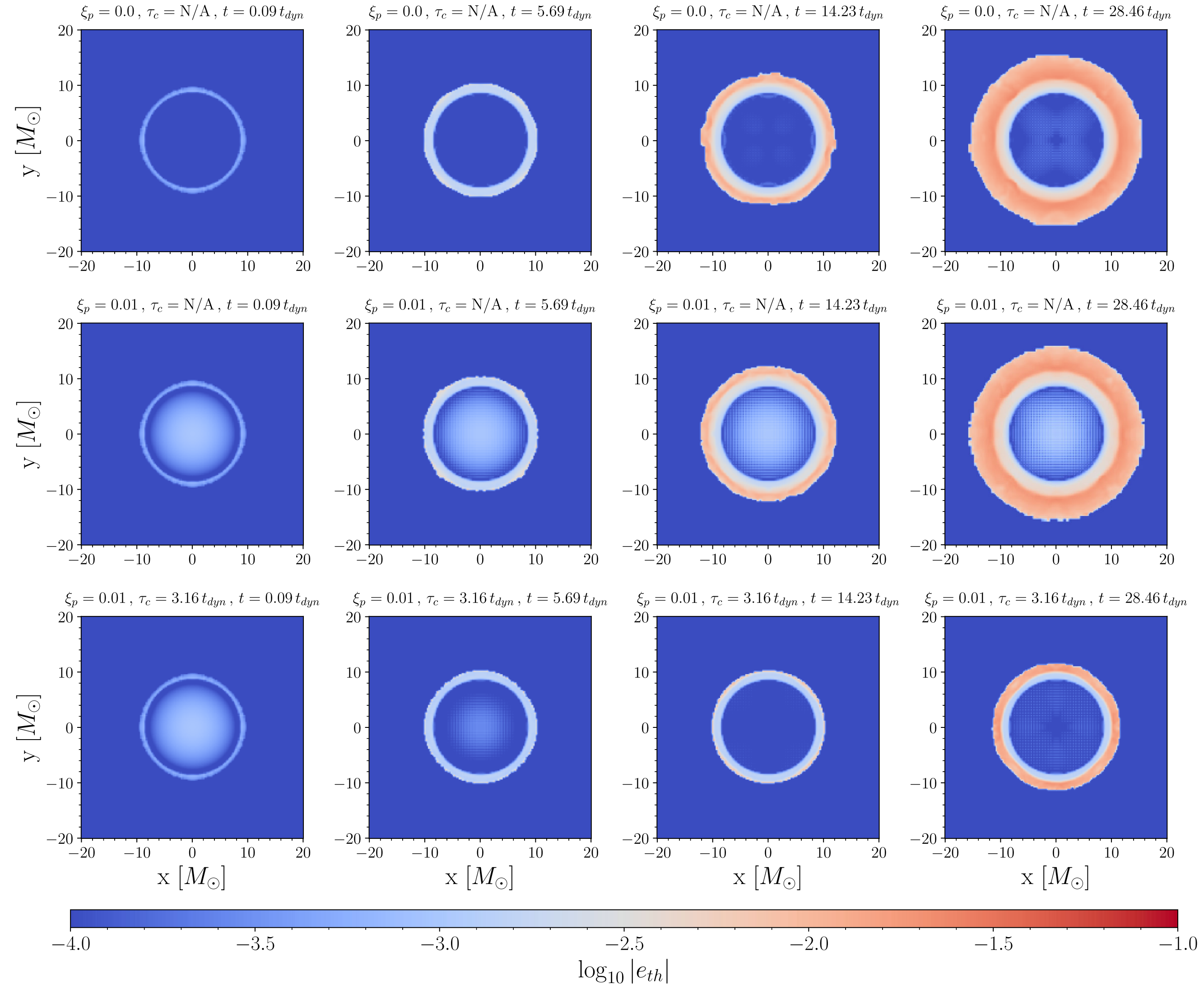

FIG. 14. The value of $|e_{\rm th}|$ is shown in two-dimensional snapshots of three simulations involving a stable NS governed by a $\Gamma = 2$ polytropic EOS with constant $k = 100M_\odot^2$, and $\rho_c = 0.001M_\odot^{-2}$. The evolution of each simulation is illustrated in a separate row. The first row describes a NS without any initial perturbation in pressure and without cooling. The second row corresponds to the case with a small pressure perturbation in the initial data and no cooling. The bottom row has the same initial data as the second row but cooling is active. The plot demonstrates that cooling is effective at removing excess heat in the bulk of the stellar matter. The stellar surface discontinuity generates heat at every time step and would require more aggressive cooling to completely cool. However, the amount of mass in that hotter region is negligible compared to that of the cold bulk of the star.

simulations are presented in the three rows, respectively. Even in the first simulation, where there is no additional thermal pressure in the initial data, small numerical errors result in the generation of some heat that grows over time. These numerical errors can also deplete heat, leading to negative $e_{\rm th}$ at some points. This is why we show the absolute value of this quantity. The initial data for this simulation contain no initial heat, as there is no heat source of $P_{\rm th}$ at the beginning. In the second simulation, the perturbation $\xi_p = 0.01$ results in heat in the initial data. This excess heat can accumulate alongside the contribution from the numerical errors over time, resulting in a relatively hotter configuration. The third simulation starts with the same amount of initial heat as the second simulation, but cooling removes the extra heat from the star. As can be seen in the bottom row of plots in Fig. 14, the initial heat and a significant portion of the heat arising from numerical errors are effectively removed after a few dynamical times.

We can also examine the evolution of $P_{\rm th}$ at the center of the star in these three simulation, as depicted in Fig. 15. In the first simulation, $P_{\rm th}$ increases over time as a result of numerical error. The value of $P_{\rm th}$ remains constant over time in the second simulation, as expected. In the last simulation, the cooling mechanism gradually decreases the

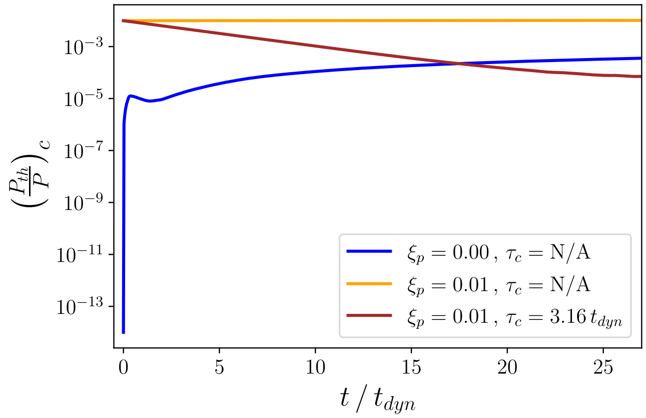

FIG. 15. The time evolution of P_{th}/P at the center of the star is shown for three different simulations. The blue curve corresponds to a simulation without any perturbation or cooling. The orange curve has no cooling but incorporates a pressure perturbation with $\xi_p = 0.01$. The dark red curve corresponds to the simulation with $\xi_p = 0.01$, but cooling is active with $\tau_c = 3.16 t_{\mathrm{dyn}}$.

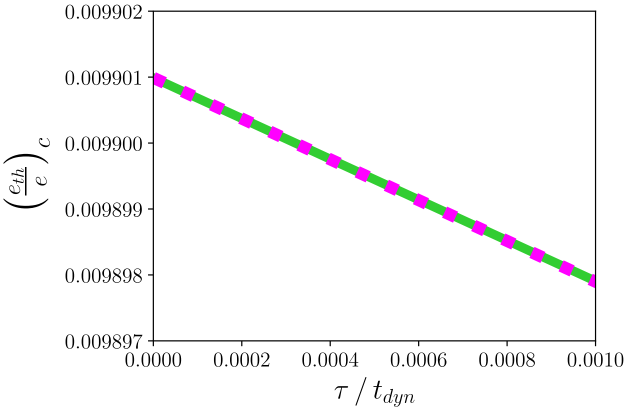

FIG. 17. The evolution of the quantity e_{th}/e at the center of a NS during the early times. The green curve represents the simulation results with $\xi_p = 0.01$ and $\tau_c = 3.16 t_{\mathrm{dyn}}$. The fitted model described by Eq. (C2) is shown by dots, with the damping timescale set to $\tau_{\mathrm{damp}} = 3.20 t_{\mathrm{dyn}}$.

value of P_{th}. After $\sim 18 t_{\mathrm{dyn}}$, the central value of P_{th} in this simulation drops below its corresponding value in both the other simulations, revealing the successful removal of heat by cooling. The positive δP also leads to a decrease in density at every point. This behavior can be seen in Fig. 16. The positive perturbation induces more pronounced oscillations in quantities such as density, similar to the oscillations that will be discussed in Appendix D for stable stars. These oscillations remain strong even after many t_{dyn}, while cooling has eliminated the majority of the heat. In this, cooling drives the maximum density to converge to its initial value and oscillate around it.

The results of these simulations indicate that cooling is successfully removing excess heat, restoring the EOS to its cold state. Having verified the functionality of the code, we test its accuracy. In other words, cooling should operate as modeled in Appendix B. To design an actual (quantitative) cooling test, we may focus on the evolution of the quantity e_{th}/e at the center over the very early times, for a simulation with $\xi_p = 0.01$ and $\tau_c = 3.16 t_{\mathrm{dyn}}$. If ρ_0 is fixed, the value of e_{th} must be decreasing as an exponential function with the proper time, as expressed by Eq. (B14). Unlike the previous plot, the evolving quantity here is shown as a function of proper time τ rather than coordinate time t. This adjustment is made due to the exponential behavior being dependent on proper time. To convert the coordinate time to proper time, the value of the lapse function is obtained at each time step, and the conversion is achieved by

$$d\tau = \alpha dt. \tag{C1}$$

Then, the result can be fitted to an exponential function characterized by a damping timescale τ_{damp} as

$$e_{\mathrm{th}} \propto \exp\left(-\frac{\tau}{\tau_{\mathrm{damp}}}\right). \tag{C2}$$

The solid curve in Fig. 17 shows the simulation results, and the dots represent the fitted model based on Eq. (C2) with $\tau_{\mathrm{damp}} = 3.20 t_{\mathrm{dyn}}$ to this curve at early times. Note that $\tau_c = \tau_{\mathrm{damp}}$ only if $d\rho_0/d\tau = 0$. Although the density changes only little in our simulations, it is not constant. Therefore, we expect that the measured τ_{damp} will deviate slightly from the expected value of τ_c. In our simulation, the difference between τ_c and τ_{damp} is only $\sim 1\%$.

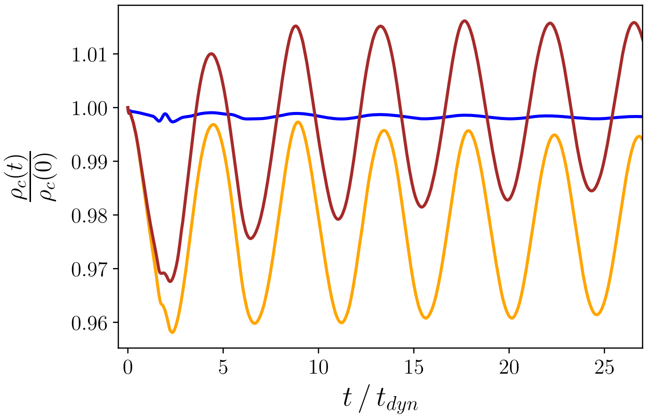

FIG. 16. Time evolution of the central density for the three simulations shown in Fig. 15, with colors having the same meaning.

APPENDIX D: STABLE STARS

In this appendix, we simulate the two stable configurations **C** and **E** in Fig. 1, representing a NS and a HS, respectively. We do this to demonstrate that our code can

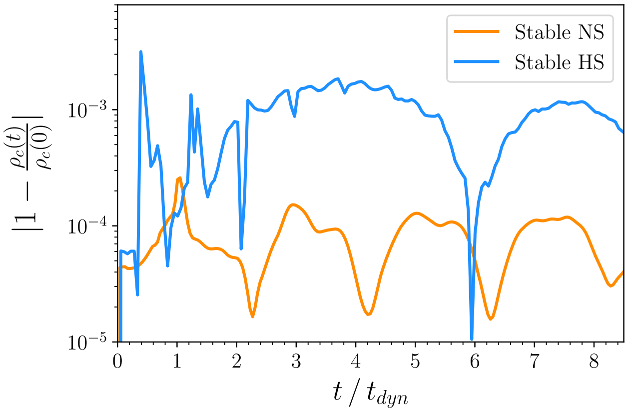

FIG. 18. Evolution of the central rest-mass density for the stable NS configuration **C** (orange) and for the stable HS configuration **E** (blue). The coordinate time t is scaled with the dynamical timescale t_{dyn}, which depends on the initial maximum density $\rho_c(0)$ and is different for the two stars. The plot demonstrates that we can accurately evolve stable compact stars with the EOSs we constructed.

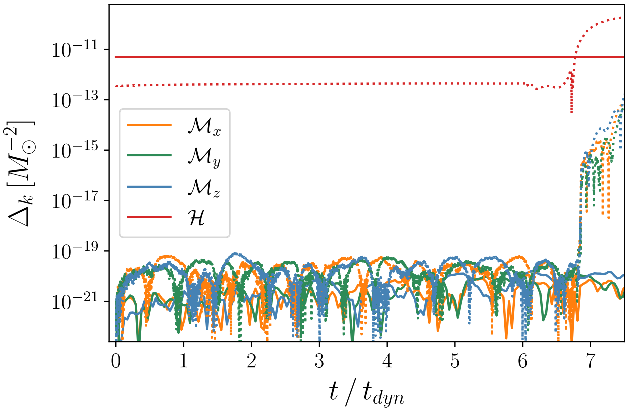

FIG. 19. The constraints as a function of time scaled by the initial dynamical timescale for the Hamiltonian constraint (represented in red) and x, y, and z components of the momentum constraint (shown in orange, green, and blue, respectively). Solid curves stand for the simulation of the stable NS configuration **C**, while dotted curves denote the collapsing WD configuration **B**. The sudden rise in Δ_k when the initial WD enters rapid collapse is unavoidable. However, the value of Δ_k remains sufficiently small throughout the simulation.

evolve stable stars and since we expect these two configurations to be the end points for a collapsing unstable WD, i.e., configuration **B**. Configuration **C** is the stable NS with a central density of $\rho_c = 6.04 \times 10^{14}\ \mathrm{g\,cm^{-3}}$ and a radius $R = 13.78$ km. Configuration **E**, on the other hand, is a stable HS with a central density of $\rho_c = 1.57 \times 10^{15}\ \mathrm{g\,cm^{-3}}$ and a radius $R = 11.40$ km.

For these simulations, the grid structure consists of eight and seven refinement levels, respectively. In both configurations, the finest resolution is set to 100 points across the initial radius of the stars. The half-side length of the coarsest box is $134.4R$ for the stable NS simulation and $67.2R$ for the stable HS simulation.

Figure 18 shows the relative deviation of the central density over time, with respect to its initial value. This figure indicates that over $8t_{\mathrm{dyn}}$ the stable NS exhibits density fluctuations of ∼0.01% at maximum, while the largest amplitude of fluctuations for the HS is ∼0.1%. Because of the transition to the more complex part of the EOS, the density evolution of the stable HS follows a less predictable pattern.

The primary conclusion drawn from these simulations is that the stable configurations of the TSs are dynamically stable indeed, and our code can accurately evolve them.

APPENDIX E: CONSTRAINTS

To ensure the accuracy of the evolution of the Einstein equations, we monitor the Hamiltonian and momentum constraint equations (see [151] for a detailed discussion on the 3 + 1 decomposition of Einstein's equations). This is important because, after perturbing our initial data, we do not resolve the constraints, so any constraint violations should remain small. In this appendix, we demonstrate that this is the case.

The absolute value of the constraint violation averaged over volume as a function of time is shown in Fig. 19 for both a stable NS (solid curves) and a collapsing WD with cooling activated from the beginning (dotted curves). The constraint violations are denoted by Δ_k. Red corresponds to the violation of the Hamiltonian constraint $\mathcal{H}$, while the momentum constraint violations, $\mathcal{M}_j$ with $j = \{x, y, z\}$, correspond to orange, green, and blue. Δ_k should remain close to zero at all time steps. As the star undergoes collapse, the computational errors increase, leading to larger values of Δ_k. Since Δ_k is a dimensionful quantity, we also show Δ_k for the stable NS simulation discussed in Appendix D for comparison. The plot demonstrates that the constraints remain well satisfied throughout the collapse. The maximum value of Δ_k remains small even in the simulations with more aggressive initial perturbations presented in this work, and it similarly occurs during the late stages of the collapse. The worst case in our simulations involved the HS with mass loss, where constraint violations are still $\Delta_k \lesssim 10^{-9} M_\odot^{-2}$.

[1] J. M. Lattimer, The nuclear equation of state and neutron star masses, Annu. Rev. Nucl. Part. Sci. **62**, 485 (2012).

[2] C. Drischler, R. J. Furnstahl, J. A. Melendez, and D. R. Phillips, How well do we know the neutron-matter equation of state at the densities inside neutron stars? A Bayesian approach with correlated uncertainties, Phys. Rev. Lett. **125**, 202702 (2020).

[3] R. Somasundaram, I. Tews, and J. Margueron, Perturbative QCD and the neutron star equation of state, Phys. Rev. C **107**, L052801 (2023).

[4] E. Epelbaum, H.-W. Hammer, and U.-G. Meissner, Modern theory of nuclear forces, Rev. Mod. Phys. **81**, 1773 (2009).

[5] R. Machleidt and D. R. Entem, Chiral effective field theory and nuclear forces, Phys. Rep. **503**, 1 (2011).

[6] I. Tews, T. Krüger, K. Hebeler, and A. Schwenk, Neutron matter at next-to-next-to-next-to-leading order in chiral effective field theory, Phys. Rev. Lett. **110**, 032504 (2013).

[7] K. Hebeler, J. M. Lattimer, C. J. Pethick, and A. Schwenk, Equation of state and neutron star properties constrained by nuclear physics and observation, Astrophys. J. **773**, 11 (2013).

[8] C. Drischler, V. Soma, and A. Schwenk, Microscopic calculations and energy expansions for neutron-rich matter, Phys. Rev. C **89**, 025806 (2014).

[9] K. Hebeler, J. D. Holt, J. Menendez, and A. Schwenk, Nuclear forces and their impact on neutron-rich nuclei and neutron-rich matter, Annu. Rev. Nucl. Part. Sci. **65**, 457 (2015).

[10] J. W. Holt and N. Kaiser, Equation of state of nuclear and neutron matter at third-order in perturbation theory from chiral effective field theory, Phys. Rev. C **95**, 034326 (2017).

[11] D. Lonardoni, I. Tews, S. Gandolfi, and J. Carlson, Nuclear and neutron-star matter from local chiral interactions, Phys. Rev. Res. **2**, 022033 (2020).

[12] C. Drischler, J. W. Holt, and C. Wellenhofer, Chiral effective field theory and the high-density nuclear equation of state, Annu. Rev. Nucl. Part. Sci. **71**, 403 (2021).

[13] M. G. Alford, L. Brodie, A. Haber, and I. Tews, Relativistic mean-field theories for neutron-star physics based on chiral effective field theory, Phys. Rev. C **106**, 055804 (2022).

[14] C. Raithel, V. Paschalidis, and F. Özel, Realistic finite-temperature effects in neutron star merger simulations, Phys. Rev. D **104**, 063016 (2021).

[15] C. A. Raithel and V. Paschalidis, Influence of stellar compactness on finite-temperature effects in neutron star merger simulations, Phys. Rev. D **108**, 083029 (2023).

[16] C. A. Raithel and V. Paschalidis, Detectability of finite-temperature effects from neutron star mergers with next-generation gravitational wave detectors, arXiv:2312.14046 [Phys. Rev. D (to be published)].

[17] G.-Q. Li, C. H. Lee, and G. E. Brown, Kaon production in heavy ion collisions and maximum mass of neutron stars, Phys. Rev. Lett. **79**, 5214 (1997).

[18] M. B. Tsang *et al.*, Constraints on the symmetry energy and neutron skins from experiments and theory, Phys. Rev. C **86**, 015803 (2012).

[19] C. J. Horowitz, Neutron rich matter in the laboratory and in the heavens after GW170817, Ann. Phys. (Amsterdam) **411**, 167992 (2019).

[20] S. Huth *et al.*, Constraining neutron-star matter with microscopic and macroscopic collisions, Nature (London) **606**, 276 (2022).

[21] E. R. Most, A. Motornenko, J. Steinheimer, V. Dexheimer, M. Hanauske, L. Rezzolla, and H. Stoecker, Probing neutron-star matter in the lab: Similarities and differences between binary mergers and heavy-ion collisions, Phys. Rev. D **107**, 043034 (2023).

[22] A. Li, G.-C. Yong, and Y.-X. Zhang, Testing the phase transition parameters inside neutron stars with the production of protons and lambdas in relativistic heavy-ion collisions, Phys. Rev. D **107**, 043005 (2023).

[23] A. Sorensen *et al.*, Dense nuclear matter equation of state from heavy-ion collisions, Prog. Part. Nucl. Phys. **134**, 104080 (2024).

[24] R. Machleidt and F. Sammarruca, Chiral EFT based nuclear forces: Achievements and challenges, Phys. Scr. **91**, 083007 (2016).

[25] I. Tews, J. Carlson, S. Gandolfi, and S. Reddy, Constraining the speed of sound inside neutron stars with chiral effective field theory interactions and observations, Astrophys. J. **860**, 149 (2018).

[26] K. Nagata, Finite-density lattice QCD and sign problem: Current status and open problems, Prog. Part. Nucl. Phys. **127**, 103991 (2022).

[27] J. M. Lattimer, Neutron stars and the nuclear matter equation of state, Annu. Rev. Nucl. Part. Sci. **71**, 433 (2021).

[28] E. V. Shuryak, Quantum chromodynamics and the theory of superdense matter, Phys. Rep. **61**, 71 (1980).

[29] L. D. McLerran, The physics of the quark—gluon plasma, Rev. Mod. Phys. **58**, 1021 (1986).

[30] J. C. Collins and M. J. Perry, Superdense matter: Neutrons or asymptotically free quarks?, Phys. Rev. Lett. **34**, 1353 (1975).

[31] H. Heiselberg and M. Hjorth-Jensen, Phases of dense matter in neutron stars, Phys. Rep. **328**, 237 (2000).

[32] D. Blaschke, D. E. Alvarez-Castillo, and S. Benic, Mass-radius constraints for compact stars and a critical endpoint, Proc. Sci. CPOD2013 (**2013**) 063 [arXiv:1310.3803].

[33] S. Benic, D. Blaschke, D. E. Alvarez-Castillo, T. Fischer, and S. Typel, A new quark-hadron hybrid equation of state for astrophysics—I. High-mass twin compact stars, Astron. Astrophys. **577**, A40 (2015).

[34] V. Paschalidis, K. Yagi, D. Alvarez-Castillo, D. B. Blaschke, and A. Sedrakian, Implications from GW170817 and I-Love-Q relations for relativistic hybrid stars, Phys. Rev. D **97**, 084038 (2018).

[35] I. F. Ranea-Sandoval, M. G. Orsaria, G. Malfatti, D. Curin, M. Mariani, G. A. Contrera, and O. M. Guilera, Effects of hadron-quark phase transitions in hybrid stars within the NJL model, Symmetry **11**, 425 (2019).

[36] G. Bozzola, P. L. Espino, C. D. Lewin, and V. Paschalidis, Maximum mass and universal relations of rotating relativistic hybrid hadron-quark stars, Eur. Phys. J. A **55**, 149 (2019).

[37] E. R. Most, L. J. Papenfort, V. Dexheimer, M. Hanauske, S. Schramm, H. Stöcker, and L. Rezzolla, Signatures of quark-hadron phase transitions in general-relativistic neutron-star mergers, Phys. Rev. Lett. **122**, 061101 (2019).

[38] A. Bauswein, N.-U. F. Bastian, D. B. Blaschke, K. Chatziioannou, J. A. Clark, T. Fischer, and M. Oertel, Identifying a first-order phase transition in neutron star mergers through gravitational waves, Phys. Rev. Lett. **122**, 061102 (2019).

[39] K. Chatziioannou and S. Han, Studying strong phase transitions in neutron stars with gravitational waves, Phys. Rev. D **101**, 044019 (2020).

[40] K. Otto, M. Oertel, and B.-J. Schaefer, Hybrid and quark star matter based on a nonperturbative equation of state, Phys. Rev. D **101**, 103021 (2020).

[41] H. Gieg, T. Dietrich, and M. Ujevic, Simulating binary neutron stars with hybrid equation of states: Gravitational waves, electromagnetic signatures, and challenges for numerical relativity, Particles **2**, 365 (2019).

[42] W.-J. Xie and B.-A. Li, Bayesian inference of the dense-matter equation of state encapsulating a first-order hadron-quark phase transition from observables of canonical neutron stars, Phys. Rev. C **103**, 035802 (2021).

[43] A. Bauswein, S. Blacker, V. Vijayan, N. Stergioulas, K. Chatziioannou, J. A. Clark, N.-U. F. Bastian, D. B. Blaschke, M. Cierniak, and T. Fischer, Equation of state constraints from the threshold binary mass for prompt collapse of neutron star mergers, Phys. Rev. Lett. **125**, 141103 (2020).

[44] A. Prakash, D. Radice, D. Logoteta, A. Perego, V. Nedora, I. Bombaci, R. Kashyap, S. Bernuzzi, and A. Endrizzi, Signatures of deconfined quark phases in binary neutron star mergers, Phys. Rev. D **104**, 083029 (2021).

[45] H. Tan, T. Dore, V. Dexheimer, J. Noronha-Hostler, and N. Yunes, Extreme matter meets extreme gravity: Ultraheavy neutron stars with phase transitions, Phys. Rev. D **105**, 023018 (2022).

[46] J. Takatsy, P. Kovacs, G. Wolf, and J. Schaffner-Bielich, What neutron stars tell about the hadron-quark phase transition: A Bayesian study, Phys. Rev. D **108**, 043002 (2023).

[47] L. R. Weih, M. Hanauske, and L. Rezzolla, Postmerger gravitational-wave signatures of phase transitions in binary mergers, Phys. Rev. Lett. **124**, 171103 (2020).

[48] M. Hanauske, L. R. Weih, H. Stöcker, and L. Rezzolla, Metastable hypermassive hybrid stars as neutron-star merger remnants: A case study, Eur. Phys. J. Spec. Top. **230**, 543 (2021).

[49] S. Haque, R. Mallick, and S. K. Thakur, Effects of onset of phase transition on binary neutron star mergers, Mon. Not. R. Astron. Soc. **527**, 11575 (2024).

[50] S. Blacker, A. Bauswein, and S. Typel, Exploring thermal effects of the hadron-quark matter transition in neutron star mergers, Phys. Rev. D **108**, 063032 (2023).

[51] U. H. Gerlach, Equation of state at supranuclear densities and the existence of a third family of superdense stars, Phys. Rev. **172**, 1325 (1968).

[52] B. Kampfer, On the possibility of stable quark and pion condensed stars, J. Phys. A **14**, L471 (1981).

[53] N. K. Glendenning and C. Kettner, Nonidentical neutron star twins, Astron. Astrophys. **353**, L9 (2000).

[54] K. Schertler, C. Greiner, J. Schaffner-Bielich, and M. H. Thoma, Quark phases in neutron stars and a third family of compact stars as a signature for phase transitions, Nucl. Phys. **A677**, 463 (2000).

[55] N. S. Ayvazyan, G. Colucci, D. H. Rischke, and A. Sedrakian, Rotating hybrid compact stars, Astron. Astrophys. **559**, A118 (2013).

[56] A. Zacchi, M. Hanauske, and J. Schaffner-Bielich, Stable hybrid stars within a SU(3) quark-meson-model, Phys. Rev. D **93**, 065011 (2016).

[57] M. Bejger, D. Blaschke, P. Haensel, J. L. Zdunik, and M. Fortin, Consequences of a strong phase transition in the dense matter equation of state for the rotational evolution of neutron stars, Astron. Astrophys. **600**, A39 (2017).

[58] M. A. R. Kaltenborn, N.-U. F. Bastian, and D. B. Blaschke, Quark-nuclear hybrid star equation of state with excluded volume effects, Phys. Rev. D **96**, 056024 (2017).

[59] M. G. Alford and A. Sedrakian, Compact stars with sequential QCD phase transitions, Phys. Rev. Lett. **119**, 161104 (2017).

[60] D. Blaschke and N. Chamel, Phases of dense matter in compact stars, Astrophysics and Space Science Library **457**, 337 (2018).

[61] D. E. Alvarez-Castillo, D. B. Blaschke, A. G. Grunfeld, and V. P. Pagura, Third family of compact stars within a nonlocal chiral quark model equation of state, Phys. Rev. D **99**, 063010 (2019).

[62] D. Blaschke, A. Ayriyan, D. E. Alvarez-Castillo, and H. Grigorian, Was GW170817 a canonical neutron star merger? Bayesian analysis with a third family of compact stars, Universe **6**, 81 (2020).

[63] A. Pfaff, H. Hansen, and F. Gulminelli, Bayesian analysis of the properties of hybrid stars with the Nambu–Jona-Lasinio model, Phys. Rev. C **105**, 035802 (2022).

[64] A. Zacchi, L. Tolos, and J. Schaffner-Bielich, Twin stars within the SU(3) chiral quark-meson model, Phys. Rev. D **95**, 103008 (2017).

[65] D. Alvarez-Castillo, A. Ayriyan, S. Benic, D. Blaschke, H. Grigorian, and S. Typel, New class of hybrid EoS and Bayesian M-R data analysis, Eur. Phys. J. A **52**, 69 (2016).

[66] J.-E. Christian, A. Zacchi, and J. Schaffner-Bielich, Classifications of twin star solutions for a constant speed of sound parameterized equation of state, Eur. Phys. J. A **54**, 28 (2018).

[67] G. Montana, L. Tolos, M. Hanauske, and L. Rezzolla, Constraining twin stars with GW170817, Phys. Rev. D **99**, 103009 (2019).

[68] M. Sieniawska, W. Turczanski, M. Bejger, and J. L. Zdunik, Tidal deformability and other global parameters of compact stars with strong phase transitions, Astron. Astrophys. **622**, A174 (2019).

[69] Z. Sharifi, M. Bigdeli, and D. Alvarez-Castillo, Studying VLOCV twin compact stars with binary mergers, Phys. Rev. D **103**, 103011 (2021).

[70] D. Sen, N. Alam, and G. Chaudhuri, Detailed analysis of the special points on $M - R$ solutions of hybrid/twin stars, Phys. Rev. D **106**, 083008 (2022).

[71] L. Tsaloukidis, P. S. Koliogiannis, A. Kanakis-Pegios, and C. C. Moustakidis, Twin stars as probes of the nuclear equation of state: Effects of rotation through the PSR J0952-0607 pulsar and constraints via the tidal deformability from the GW170817 event, Phys. Rev. D **107**, 023012 (2023).

[72] E. Annala, T. Gorda, A. Kurkela, J. Nättilä, and A. Vuorinen, Evidence for quark-matter cores in massive neutron stars, Nat. Phys. **16**, 907 (2020).

[73] E. Annala, T. Gorda, E. Katerini, A. Kurkela, J. Nättilä, V. Paschalidis, and A. Vuorinen, Multimessenger constraints for ultradense matter, Phys. Rev. X **12**, 011058 (2022).

[74] J. J. Li, A. Sedrakian, and M. Alford, Ultracompact hybrid stars consistent with multimessenger astrophysics, Phys. Rev. D **107**, 023018 (2023).

[75] R. Essick, I. Legred, K. Chatziioannou, S. Han, and P. Landry, Phase transition phenomenology with nonparametric representations of the neutron star equation of state, Phys. Rev. D **108**, 043013 (2023).

[76] Y. Yamamoto, N. Yasutake, and T. A. Rijken, Quark phases in neutron stars consistent with implications from NICER observations, Phys. Rev. C **108**, 035811 (2023).

[77] Z. Lin and A. Steiner, Indication of sharp and strong phase-transitions from NICER observations, arXiv:2310.01619.

[78] R. Somasundaram, I. Tews, and J. Margueron, Investigating signatures of phase transitions in neutron-star cores, Phys. Rev. C **107**, 025801 (2023).

[79] L. Brandes, W. Weise, and N. Kaiser, Evidence against a strong first-order phase transition in neutron star cores: Impact of new data, Phys. Rev. D **108**, 094014 (2023).

[80] A. Drago and G. Pagliara, Merger of two neutron stars: Predictions from the two-families scenario, Astrophys. J. Lett. **852**, L32 (2018).

[81] G. F. Burgio, A. Drago, G. Pagliara, H. J. Schulze, and J. B. Wei, Are small radii of compact stars ruled out by GW170817/AT2017gfo?, Astrophys. J. **860**, 139 (2018).

[82] R. Essick, P. Landry, and D. E. Holz, Nonparametric inference of neutron star composition, equation of state, and maximum mass with GW170817, Phys. Rev. D **101**, 063007 (2020).

[83] R. De Pietri, A. Drago, A. Feo, G. Pagliara, M. Pasquali, S. Traversi, and G. Wiktorowicz, Merger of compact stars in the two-families scenario, Astrophys. J. **881**, 122 (2019).

[84] T. Gorda, K. Hebeler, A. Kurkela, A. Schwenk, and A. Vuorinen, Constraints on strong phase transitions in neutron stars, Astrophys. J. **955**, 100 (2023).

[85] J. Jie Li, A. Sedrakian, and M. Alford, Hybrid star models in the light of new multi-messenger data, Astrophys. J. **967**, 116 (2024).

[86] K. Maslov, N. Yasutake, A. Ayriyan, D. Blaschke, H. Grigorian, T. Maruyama, T. Tatsumi, and D. N. Voskresensky, Hybrid equation of state with pasta phases and third family of compact stars, Phys. Rev. C **100**, 025802 (2019).

[87] N. K. Glendenning, *Compact Stars: Nuclear Physics, Particle Physics, and General Relativity*, Astronomy and Astrophysics Library (Springer, New York, 1997).

[88] F. Weber, *Pulsars as Astrophysical Laboratories for Nuclear and Particle Physics* (Institute of Physics, Bristol, 1999).

[89] S. L. Shapiro and S. A. Teukolsky, *Black Holes, White Dwarfs, and Neutron Stars: The Physics of Compact Objects* (Wiley-VCH Verlag, Berlin, 1983).

[90] R. Kippenhahn, A. Weigert, and A. Weiss, *Stellar Structure and Evolution*, Astronomy and Astrophysics Library (Springer, New York, 2012).

[91] P. L. Espino and V. Paschalidis, Fate of twin stars on the unstable branch: Implications for the formation of twin stars, Phys. Rev. D **105**, 043014 (2022).

[92] S. A. Colgate, A. G. Petschek, and J. T. Kriese, The luminosity of type I supernovae, Astrophys. J. Lett. **237**, L81 (1980).

[93] G. F. Burgio, H. J. Schulze, I. Vidana, and J. B. Wei, Neutron stars and the nuclear equation of state, Prog. Part. Nucl. Phys. **120**, 103879 (2021).

[94] T. Kojo, QCD equations of state and speed of sound in neutron stars, AAPPS Bull. **31**, 11 (2021).

[95] G. Baym, T. Hatsuda, T. Kojo, P. D. Powell, Y. Song, and T. Takatsuka, From hadrons to quarks in neutron stars: A review, Rep. Prog. Phys. **81**, 056902 (2018).

[96] J. S. Read, B. D. Lackey, B. J. Owen, and J. L. Friedman, Constraints on a phenomenologically parameterized neutron-star equation of state, Phys. Rev. D **79**, 124032 (2009).

[97] L. Lindblom, Spectral representations of neutron-star equations of state, Phys. Rev. D **82**, 103011 (2010).

[98] M. F. O'Boyle, C. Markakis, N. Stergioulas, and J. S. Read, Parametrized equation of state for neutron star matter with continuous sound speed, Phys. Rev. D **102**, 083027 (2020).

[99] V. Paschalidis, Z. Etienne, Y. T. Liu, and S. L. Shapiro, Head-on collisions of binary white dwarf–neutron stars: Simulations in full general relativity, Phys. Rev. D **83**, 064002 (2011).

[100] G. Colucci and A. Sedrakian, Equation of state of hypernuclear matter: Impact of hyperon–scalar-meson couplings, Phys. Rev. C **87**, 055806 (2013).

[101] E. Witten, Cosmic separation of phases, Phys. Rev. D **30**, 272 (1984).

[102] P. Haensel, J. L. Zdunik, and R. Schaefer, Strange quark stars, Astron. Astrophys. **160**, 121 (1986).

[103] C. Alcock, E. Farhi, and A. Olinto, Strange stars, Astrophys. J. **310**, 261 (1986).

[104] J. L. Zdunik, Strange stars: Linear approximation of the EOS and maximum QPO frequency, Astron. Astrophys. **359**, 311 (2000).

[105] J. W. Negele and D. Vautherin, Neutron star matter at subnuclear densities, Nucl. Phys. **A207**, 298 (1973).

[106] G. Baym, C. Pethick, and P. Sutherland, The ground state of matter at high densities: Equation of state and stellar models, Astrophys. J. **170**, 299 (1971).

[107] D. E. Alvarez-Castillo and D. B. Blaschke, High-mass twin stars with a multipolytrope equation of state, Phys. Rev. C **96**, 045809 (2017).

[108] P. Demorest, T. Pennucci, S. Ransom, M. Roberts, and J. Hessels, Shapiro delay measurement of a two solar mass neutron star, Nature (London) **467**, 1081 (2010).

[109] J. Antoniadis *et al.*, A massive pulsar in a compact relativistic binary, Science **340**, 6131 (2013).

[110] E. Fonseca *et al.*, The NANOGrav nine-year data set: Mass and geometric measurements of binary millisecond pulsars, Astrophys. J. **832**, 167 (2016).

[111] H. T. Cromartie *et al.* (NANOGrav Collaboration), Relativistic Shapiro delay measurements of an extremely massive millisecond pulsar, Nat. Astron. **4**, 72 (2019).

[112] E. Fonseca *et al.*, Refined mass and geometric measurements of the high-mass PSR J0740 + 6620, Astrophys. J. Lett. **915**, L12 (2021).

[113] S. M. Carroll, *Spacetime and Geometry: An Introduction to General Relativity* (Cambridge University Press, Cambridge, England, 2019).

[114] A. Akmal, V. R. Pandharipande, and D. G. Ravenhall, The equation of state of nucleon matter and neutron star structure, Phys. Rev. C **58**, 1804 (1998).

[115] S. A. Bludman and M. A. Ruderman, Possibility of the speed of sound exceeding the speed of light in ultradense matter, Phys. Rev. **170**, 1176 (1968).

[116] M. G. Alford, S. Han, and M. Prakash, Generic conditions for stable hybrid stars, Phys. Rev. D **88**, 083013 (2013).

[117] C. C. Moustakidis, T. Gaitanos, C. Margaritis, and G. A. Lalazissis, Bounds on the speed of sound in dense matter, and neutron star structure, Phys. Rev. C **95**, 045801 (2017); **95**, 059904(E) (2017).

[118] B. Reed and C. J. Horowitz, Large sound speed in dense matter and the deformability of neutron stars, Phys. Rev. C **101**, 045803 (2020).

[119] A. Kurkela, P. Romatschke, and A. Vuorinen, Cold quark matter, Phys. Rev. D **81**, 105021 (2010).

[120] F. Özel and P. Freire, Masses, radii, and the equation of state of neutron stars, Annu. Rev. Astron. Astrophys. **54**, 401 (2016).

[121] P. Haensel, M. Bejger, M. Fortin, and L. Zdunik, Rotating neutron stars with exotic cores: Masses, radii, stability, Eur. Phys. J. A **52**, 59 (2016).

[122] C. A. Raithel, Constraints on the neutron star equation of state from GW170817, Eur. Phys. J. A **55**, 80 (2019).

[123] D. Radice, S. Bernuzzi, and A. Perego, The dynamics of binary neutron star mergers and GW170817, Annu. Rev. Nucl. Part. Sci. **70**, 95 (2020).

[124] V. Paschalidis, Y. T. Liu, Z. Etienne, and S. L. Shapiro, The merger of binary white dwarf–neutron stars: Simulations in full general relativity, Phys. Rev. D **84**, 104032 (2011).

[125] F. Loffler *et al.*, The Einstein Toolkit: A community computational infrastructure for relativistic astrophysics, Classical Quantum Gravity **29**, 115001 (2012).

[126] L. Werneck *et al.*, The Einstein Toolkit, to find out more, visit http://einsteintoolkit.org (2023).

[127] T. Goodale, G. Allen, G. Lanfermann, J. Massó, T. Radke, E. Seidel, and J. Shalf, The Cactus framework and toolkit: Design and applications, in *Vector and Parallel Processing—VECPAR'2002, 5th International Conference, Lecture Notes in Computer Science* (Springer, Berlin, 2003).

[128] The simulation factory, https://simfactory.org.

[129] E. Schnetter, S. H. Hawley, and I. Hawke, Evolutions in 3-D numerical relativity using fixed mesh refinement, Classical Quantum Gravity **21**, 1465 (2004).

[130] G. Bozzola, KUIBIT: Analyzing Einstein Toolkit simulations with Python, J. Open Source Software **6**, 3099 (2021).

[131] N. Stergioulas and J. L. Friedman, Comparing models of rapidly rotating relativistic stars constructed by two numerical methods, Astrophys. J. **444**, 306 (1995).

[132] N. Stergioulas, Rotating stars in relativity, Living Rev. Relativity **6**, 3 (2003).

[133] T. W. Baumgarte and S. L. Shapiro, On the numerical integration of Einstein's field equations, Phys. Rev. D **59**, 024007 (1998).

[134] M. Shibata and T. Nakamura, Evolution of three-dimensional gravitational waves: Harmonic slicing case, Phys. Rev. D **52**, 5428 (1995).

[135] U. Sperhake, Binary black-hole evolutions of excision and puncture data, Phys. Rev. D **76**, 104015 (2007).

[136] C. Bona, J. Masso, E. Seidel, and J. Stela, A new formalism for numerical relativity, Phys. Rev. Lett. **75**, 600 (1995).

[137] M. Alcubierre, B. Bruegmann, P. Diener, M. Koppitz, D. Pollney, E. Seidel, and R. Takahashi, Gauge conditions for long term numerical black hole evolutions without excision, Phys. Rev. D **67**, 084023 (2003).

[138] Z. B. Etienne, V. Paschalidis, R. Haas, P. Mösta, and S. L. Shapiro, IllinoisGRMHD: An open-source, user-friendly GRMHD code for dynamical spacetimes, Classical Quantum Gravity **32**, 175009 (2015).

[139] Z. B. Etienne, Cactus code thorn IllinoisGRMHD, https://github.com/zachetienne/nrpytutorial/tree/master/IllinoisGRMHD.

[140] M. Hanauske, Z. S. Yilmaz, C. Mitropoulos, L. Rezzolla, and H. Stöcker, Gravitational waves from binary compact star mergers in the context of strange matter, EPJ Web Conf. **171**, 20004 (2018).

[141] N. K. Largani, T. Fischer, A. Sedrakian, M. Cierniak, D. E. Alvarez-Castillo, and D. B. Blaschke, Universal relations for rapidly rotating cold and hot hybrid stars, Mon. Not. R. Astron. Soc. **515**, 3539 (2022).

[142] I. A. Rather, U. Rahaman, M. Imran, H. C. Das, A. A. Usmani, and S. K. Patra, Rotating neutron stars with quark cores, Phys. Rev. C **103**, 055814 (2021).

[143] K. Miao and Z. Xiaoping, Thermal evolution of rotating hybrid stars, Mon. Not. R. Astron. Soc. **375**, 1503 (2007).

[144] J. P. Carlomagno, G. A. Contrera, A. G. Grunfeld, and D. Blaschke, Hybrid isentropic twin stars, arXiv:2406.17193.

[145] I. Bombaci, D. Logoteta, I. Vidaña, and C. Providência, Quark matter nucleation in neutron stars and astrophysical implications, Eur. Phys. J. A **52**, 58 (2016).

[146] V. Paschalidis, M. MacLeod, T. W. Baumgarte, and S. L. Shapiro, Merger of white dwarf-neutron star binaries: Prelude to hydrodynamic simulations in general relativity, Phys. Rev. D **80**, 024006 (2009).

[147] A. Bauswein and S. Blacker, Impact of quark deconfinement in neutron star mergers and hybrid star mergers, Eur. Phys. J. Spec. Top. **229**, 3595 (2020).

[148] R. L. Arnowitt, S. Deser, and C. W. Misner, The dynamics of general relativity, Gen. Relativ. Gravit. **40**, 1997 (2008).

[149] M. D. Duez, Y. T. Liu, S. L. Shapiro, and B. C. Stephens, Relativistic magnetohydrodynamics in dynamical spacetimes: Numerical methods and tests, Phys. Rev. D **72**, 024028 (2005).

[150] B. C. Stephens, S. L. Shapiro, and Y. T. Liu, Collapse of magnetized hypermassive neutron stars in general relativity: Disk evolution and outflows, Phys. Rev. D **77**, 044001 (2008).

[151] T. W. Baumgarte and S. L. Shapiro, *Numerical Relativity: Solving Einstein's Equations on the Computer* (Cambridge University Press, Cambridge, England, 2010).